

THESIS FOR THE DEGREE OF DOCTOR OF PHILOSOPHY

Coated Ferritic Stainless Steels as Interconnects in Solid Oxide Fuel Cells

Material Development and Electrical Properties

Jan Gustav Grolig



Department of Chemistry and Chemical Engineering
CHALMERS UNIVERSITY OF TECHNOLOGY
Gothenburg, Sweden 2015

Coated Ferritic Stainless Steels as Interconnects in Solid Oxide Fuel Cells

Material Development and Electrical Properties

Jan Gustav Grolig

ISBN: 978-91-7597-234-3

© Jan Gustav Grolig, 2015.

Doktorsavhandlingar vid Chalmers Tekniska Högskola

Ny serie Nr. 3915

ISSN: 0346-718X

Department of Chemical and Chemical Engineering

Division of Energy and Materials

Environmental Inorganic Chemistry

The High Temperature Corrosion Centre

Chalmers University of Technology

SE - 412 96 Gothenburg, Sweden

Phone + 46 (0)31 772 2828

Printed by Chalmers Reproservice

Chalmers University of Technology

Gothenburg, Sweden 2015

Cover: Scheme of ASR characterization used in this thesis.

Coated Ferritic Stainless Steels as Interconnects in Solid Oxide Fuel Cells

Material Development and Electrical Properties

Jan Gustav Grolig

Department of Chemistry and Chemical Engineering

Chalmers University of Technology

Abstract

Solid oxide fuel cells (SOFCs) are attracting increasing interest as devices with potential uses in decentralized and clean electricity and heat production. Several challenges with respect to materials have to be overcome to achieve efficiencies and life-spans that are sufficient for long-term applications.

An important element of an SOFC stack is the interconnect component, which connects two adjacent fuel cell elements. Interconnects, which are commonly composed of ferritic stainless steels, have to be corrosion-resistant, mechanically stable, good electrical conductors and cost-optimized.

This work aimed to investigate economic solutions for interconnect materials and to understand the underlying mechanisms of degradation and electrical conduction of these materials. Mainly two substrates, a commercially available steel (AISI 441) and a ferritic stainless steel that was optimized for an SOFC application (Sandvik Sanergy HT) were combined with different barrier coatings and exposed to a cathode-side atmosphere. A method was developed that allows for the electrical characterization of promising material systems and model alloys, thereby facilitating a fundamental understanding of the dominant electrical conduction processes of the oxide scales that grow on interconnects. The AISI 441 steel coated with reactive elements and cobalt showed good corrosion and chromium evaporation profiles, while AISI 441 coated with cerium and cobalt also had promising electrical properties. The Sanergy HT steel was examined with coatings of copper and iron and copper and manganese, respectively. The corrosion and chromium evaporation profiles of Sanergy HT were improved by coating with copper and iron. The copper and iron-coated Sanergy HT showed lower area specific resistance values than cobalt-coated Sanergy HT. Chromia, which is the main constituent of oxide scales, was synthesized using different methods. The electrical properties of chromia were found to be sensitive to not only impurities, but also heat treatment. Finally the electrical properties of cobalt- and cobalt cerium-coated Sanergy HT steels were investigated. It was revealed that the addition of cerium improved the conductivity of the interconnect by both slowing down chromia growth and preventing the outward diffusion of iron into the spinel.

Keywords: SOFC, ASR, Interconnects, High Temperature Corrosion

APPENDED PAPERS

The thesis is based on the following articles:

- J. G. Grolig, J. Froitzheim and J.-E. Svensson. Coated Stainless Steel 441 as Interconnect Material for Solid Oxide Fuel Cells: Oxidation Performance and Chromium Evaporation *Journal of Power Sources*, Volume 248 (2014); pages 1007-1013, doi:10.1016/j.jpowsour.2013.08.089
- J. G. Grolig, H. Abdesselam, M. Gas, H. F. Windisch, J. Froitzheim and J.-E. Svensson. Copper Based Conversion Coatings on Ferritic Stainless Strip Steel as Solid Oxide Fuel Cell Interconnects: Oxidation Performance and Chromium Evaporation *ECS Transactions*, Volume 57 (2013), Issue 1; pages 2339-2347.
- J. G. Grolig, J. Froitzheim and J.-E. Svensson. Coated Stainless Steel 441 as Interconnect Material for Solid Oxide Fuel Cells: Evolution of electrical properties *Journal of Power Sources*, Volume 284 (2015); pages 321-327, doi:10.1016/j.jpowsour.2015.03.029
- J. G. Grolig, P. Alnegren, J. Froitzheim and J.-E. Svensson. Copper Iron Conversion Coating for Solid Oxide Fuel Cell Interconnects *Journal of Power Sources*, accepted for publication.
- J. G. Grolig, J. Froitzheim and J.-E. Svensson. Effect of Cerium on the Electrical Properties of a Cobalt Conversion Coating for Solid Oxide Fuel Cell Interconnects - a Study using Impedance Spectroscopy *Electrochimica Acta*, submitted.
- J. G. Grolig, M. Sattari, P. Alnegren, J. Froitzheim and J.-E. Svensson. Electric Properties of Chromia of different Origin manuscript.

Statement of author's contribution

For all papers I was the main author and planned the experimental matrix. In paper I I did the main part of the scientific writing and all the experimental work, except the FIB preparation, that was performed by Dr. M. Sattari. In Paper II most of the experiments were performed by H. Abdesselam and M. Gas and I did some of the experiments and the scientific writing. In paper III I did the all experimental work and scientific writing. In paper IV I did the scientific writing and all experimental work,

except some of the microstructural analysis which was performed by P. Alnegren. In paper V I did the all experimental work and scientific writing. In paper VI I did the scientific writing and all experimental work, except some of the microstructural analysis, which was performed by M. Sattari and P. Alnegren.

LIST OF ACRONYMS

ASR	Area Specific Resistance
CGO	Gadolina doped Ceria
CTE	Coefficient of Thermal Expansion
EDX	Energy Dispersive X-ray analysis
FIB	Focused Ion Beam
HTC	High Temperature Corrosion Centre at Chalmers University of Technology
HTPEM	High Temperature Polymeric Membrane Fuel Cell
KMC	Kinetic Monte Carlo Simulation
LSC	Scandia Doped Lanthanum Chromite
LSCF	Strontium Iron Doped lanthanum cobaltite
LSM	Strontium Doped Lanthanum Magnetite
PAFC	Phosphoric Acid Fuel Cell
PEM	Polymeric Membrane Fuel Cell
RE	Reactive Element
SEM	Scanning Electron Microscopy
SOFC	Solid Oxide Fuel Cell
TEM	Transmission Electron Microscopy
XRD	X-Ray Diffractometry
YSZ	Yttria stabilized Zirconia

CONTENTS

CHAPTER 1 – INTRODUCTION	1
1.1 Aims of the thesis	2
CHAPTER 2 – THEORY	3
2.1 Solid Oxide Fuel Cells	3
2.1.1 Electrolyte materials	4
2.1.2 Electrode materials	6
Anode materials	6
Cathode materials	6
2.1.3 Interconnects	7
Ceramic interconnect materials	8
Ferritic stainless steels	8
2.2 Corrosion of metals	8
2.2.1 Thermodynamics	8
2.2.2 Kinetics	9
Parabolic mechanism	11
Logarithmic mechanism	11
Linear mechanism	12
Break-away corrosion	12
2.3 Interconnect-related corrosion challenges	12
2.3.1 Corrosion	12
Reactive Elements	13
Reactive Element coatings	13
2.3.2 Chromium evaporation	13
Coatings for preventing Chromium evaporation	14
2.3.3 Electrical conduction of oxide scales	14
Electric properties of chromia	15
Electric properties of spinels	17
CHAPTER 3 – MATERIALS AND METHODS	19
3.1 Investigated materials	19
3.2 Sample preparation	20
3.3 Exposure	20
3.3.1 Denuder technique	21
3.4 Analytical techniques	22
3.4.1 Scanning electron microscopy	22

Secondary electrons	22
Back-scattered electrons	24
Energy dispersive X-Ray analysis	24
Focused Ion Beam milling	24
3.4.2 X-ray diffraction	24
3.4.3 Electrical Characterization	25
CHAPTER 4 – RESULTS AND DISCUSSION	27
4.1 Corrosion and chromium evaporation	27
4.1.1 Chromium evaporation measurement validation	27
4.1.2 AISI 441 with different coatings	28
Gravimetric measurements and chromium evaporation	28
Microstructural evolution	30
4.1.3 Sanergy HT with copper based conversion coatings	39
4.1.4 Mass gain	39
4.1.5 Chromium evaporation	39
4.1.6 Microstructural evolution	40
4.1.7 Alternative coatings for chromium retention	44
4.2 Electrical properties	45
4.2.1 Electrical properties of chromia	46
4.2.2 AISI 441 coated with cobalt cerium	47
4.2.3 Effect of cerium in a cobalt coating	51
4.2.4 Copper iron spinel coating on Sanergy HT	56
4.2.5 Uncoated substrate materials	58
4.2.6 Conclusion on electrical properties	59
CHAPTER 5 – SUMMARY AND OUTLOOK	63
REFERENCES	65
PAPER I	73
PAPER II	83
PAPER III	95
PAPER IV	105
PAPER V	127
PAPER VI	147

ACKNOWLEDGEMENTS

This thesis would not have been possible without the help of many people and I am very grateful to have received support in various forms.

First of all, I would like to thank my supervisor Prof. Jan-Erik Svensson for offering me this PhD position, for his encouragement, and for letting me buy all the equipment needed for my work. You have given me a large degree of freedom to steer my research and I appreciate that very much. Dr. Jan Froitzheim, my co-supervisor, is acknowledged for always being available when I had problems and for valuable inputs to my work. I also would like to thank him for leading the project and taking care of all the organizational issues associated with the SOFC research.

Furthermore, I would like to thank Prof. Lars-Gunnar Johansson for being my examiner and for supporting me with his scientific knowledge and input. Prof. Sten Eriksson is acknowledged for being my director of studies. Prof. Itai Panas has been a true source of inspiration and I appreciate the many discussions we have had - thank you!

A big thanks goes to my fellow co-workers in The Fuel Cell Group, Christine, Gert, Hannes, Maria, Mohammad, Patrik, and Rakshith, for supporting me on various issues, creating a great team spirit and for successfully withstanding my personality. Patrik, who shared an office with me, was always the first person to talk to whenever new ideas came up and I appreciate the open discussions culture we have had. Rakshith, who has been much more than flat-mate, is acknowledged for numerous open, useful and non-useful discussions. Moreover, I would like to thank Hannes for being a role model for hard and focused work, and for being a constantly positive spirit in relation to my work.

In addition, I would like to thank the entire team of the High Temperature Corrosion Center and Environmental Inorganic Chemistry for the work experience of the last four years. The group of Electrochemistry of Prof. Elisabet Ahlberg and also the Oxide group of Sten Eriksson are acknowledged for providing help, a laboratory and instrumentation for the electrical characterization and studies on oxide materials.

I am grateful to Esa Väänänen, Torbjörn Jönsson and Erik Brunius for their great support in building and fixing new laboratory equipment. Furthermore, I thank San-

dra Gustafson for running OOMK in the way that she does and helping me with all the administration issues. Charlotte Bouveng is gratefully acknowledged for the assistance she afforded me in finding a flat and for helping me through different administrative challenges.

During my time in Sweden I have made friends who made my life sweeter: I thank Adam, Arnar, Erik, Gustaf, Martin, Melanie, Niklas, Luciano, Ole-Martin and Thomas for helping me get to the point where I am now.

I also would like to thank my family for supporting me in my, not always understandable, decision to pursue a PhD in Sweden. Finally, Tuule: You are great - without you, it would have been just half the fun!

CHAPTER 1

Introduction

Global warming is currently, and will remain so for decades, one of the most important challenges facing humanity. Increasing levels of CO₂ emissions have been identified as one of the major causes of the greenhouse effect. The need for reductions in CO₂ emissions, combined with the projected shortages of fossil fuels, promotes demand for new technologies that that will enable clean, more effective, and preferably decentralized, energy and heat production.

Solid oxide fuel cells (SOFCs) represent an important part of the strategy to meet this demand. SOFCs, which can have electrical efficiencies of up to 60 %, and overall system efficiency of over 90 % allow for the flexible and decentralized production of electricity and heat. SOFCs convert the chemical energy stored in the fuel directly into electricity, without combustion. Since they can operate using existing fuels, the obstacles to market implementation are less severe than those faced by other fuel cell technologies, and the several pilot plants that are already in operation with varying power outputs have demonstrated the feasibility of the SOFC concept successfully [1]. In addition, Combined Heat and Power units (CHPs) for residential applications have attracted increasing interest [2, 3].

Several material challenges have to be solved prior to the large-scale industrial production and implementation of SOFCs. With the emergence of more (cost-)effective catalysts and economic production methods, fuel cell interconnects have attracted interest in the research community. Interconnects are used to combine several fuel cell elements into a stack, and they contribute significantly to the overall cost of the stack [4]. Ferritic stainless steels are regarded as choice materials for interconnects [5]. The major technical obstacles facing the adoption of ferritic stainless steel interconnects are: high temperature corrosion; the volatilization of chromium; and increasing electrical resistance, due to oxidation, over the lifetime of the material.

Tailor-made alloys have been developed to address these issues and highly effective coatings, ranging in thickness from sub micrometers to micrometers, can be applied to improve further the properties of these materials. A major drawback of these solutions is the cost, which means that either cheaper alloys have to be used or the coatings have

to be modified to be more cost-effective. Another challenge associated with the development of new interconnects is enabling the characterization of different materials in terms of the three main degradation mechanisms, to allow the benchmarking of different candidate materials and elucidation of the degradation mechanisms. Corrosion experiments that simulate the environment of the fuel cell facilitate quantification of the degradation process. In this context, a method developed at Chalmers University of Technology, termed the denuder technique, enables time-resolved measurements of evaporated chromium. The quantification of the electrical resistance of interconnect materials remains, in contrast to the previous mentioned methods, a major challenge.

1.1 Aims of the thesis

The aims of this thesis are two-fold. The first aim is to investigate the corrosion mechanisms and compare chromium evaporation performances of new substrate/coating combinations with those of state-of-the-art steels. For this purpose, stainless steel AISI 441 was used with state-of-the-art coatings, and new coatings were developed for a state-of-the-art substrate material, Sandvik Sanergy HT.

The second aim is to examine the electronic properties of promising candidate materials towards the goal of interconnect applications. Thus, substrate/coating combinations with demonstrated potential from the first part of the thesis work, as well as substrate/coating combinations from previous investigations at HTC, were selected for electrical characterization. The goals were to develop a suitable test method and to understand the electrical conduction mechanisms of these materials. In addition, model systems for chromia were used to relate the behaviors of the tested materials to different oxide layers.

2.1 Solid Oxide Fuel Cells

Solid Oxide Fuel Cells (SOFCs) convert electrical energy directly into electricity through a reaction between a fuel (such as hydrogen) and oxygen, without combustion. The operation of these cells is based on an oxygen-ion-conducting electrolyte in combination with mixed conducting electrodes. Since the working principle of an SOFC is not a Carnot process, they can achieve higher efficiencies than conventional combustion engines. In addition, fuel cells work almost silently and produce less pollution (depending on the fuel used). Consequently, SOFCs are promising devices for a future hydrogen-based economy [6].

The working principle of an SOFC (Figure 2.1) involves a fuel, in this case hydrogen, which is oxidized at the anode side and forms water. The anode side reaction is described by Equation 2.1. The released electrons are transferred through an external circuit to the cathode side. On the cathode side (see Equation 2.2), oxygen takes up these electrons and is reduced, with the formed oxygen ions diffusing through the electrolyte and reacting on the anode side with the hydrogen (the overall reaction in Equation 2.3). The electrons that are transferred through the external circuit can be used to drive an electric load [6].



Apart from SOFCs, other types of fuel cells are available. Table 2.1 lists some of the most important fuel cell types and their common characteristics. In contrast to most

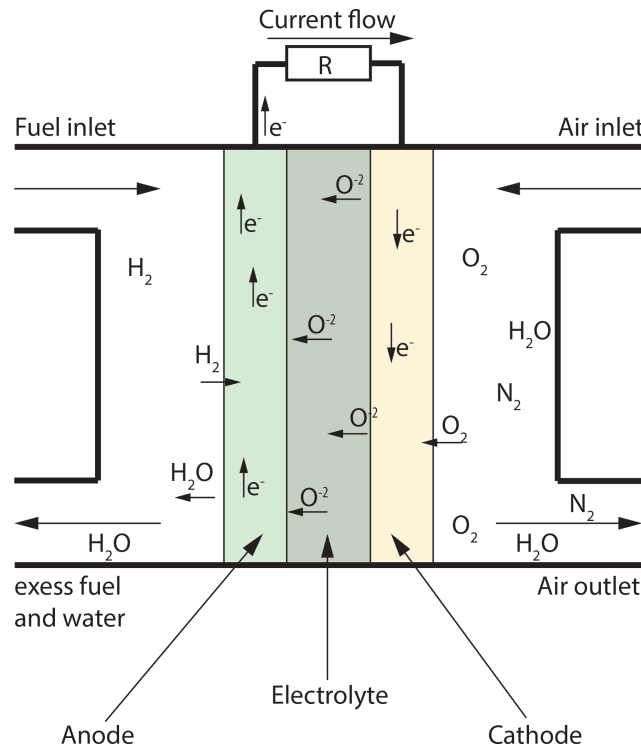


Figure 2.1: Working principle of a solid oxide fuel cell.

of the other fuel cell types, SOFCs do not require purified hydrogen as fuel, as they can run on almost any hydrocarbon fuel. Their relatively high operational temperatures make SOFCs highly suitable for stationary operation, with preferably a low number of start-up/shut-down cycles. In contrast, Polymeric Membrane (PEM) and High-Temperature Polymeric Membrane (HTPEM) fuel cells allow short start-up/shut-down times, and consequently are better suited to mobile applications. However, since they utilize platinum catalysts, which are sensitive to carbon monoxide, they require highly purified fuels and their up-scaling will be limited [6]. There are different material requirements for the different components of an SOFC, which are described in more detail in the following sections.

2.1.1 Electrolyte materials

The electrolyte in an SOFC has to be: conductive for oxygen ions; nonconductive for electrons; and stable in both oxidizing and reducing environments [7]. The most commonly used electrolyte is Yttria-Stabilized Zirconia (YSZ), although other electrolytes, such as Gadolina-Doped Ceria (CGO), have also been reported as being effective in SOFCs. At temperatures of up to 1170°C undoped zirconia has a monoclinic crystal structure; by doping zirconia with yttria or other aliovalent oxides, oxygen vacancies are introduced and the crystal structure changes to the cubic fluorite structure [7, 8]. The oxygen conductivity of YSZ can be increased by increasing the

Type	Temp. °C	Fuel	Electrolyte	Mobile ion	Advantages	Disadvantages
PEM (polymeric membrane fuel cell)	70 - 110	Hydrogen	Sulfonated polymers (Nafion®)	H^+	quick start up	high purity fuels required, platinum catalysts
HTEPM (high temperature polymeric membrane fuel cell)	150 - 200	Hydrogen	Phosphoric acid doped polybenzimidazole (PBI)	H^+	quick start up	phosphoric acid release, platinum catalysts
PAFC (phosphoric acid fuel cell)	150 - 250	Hydrogen	Phosphoric acid	H^+	high tolerance against CO	only constant operation
SOFC (solid oxide fuel cell)	600 - 850	Hydrocarbons, CO	YSZ, CGO	O^{2-}	high fuel tolerance	no quick start up, high operation temperatures

Table 2.1: Common fuel cell types and their characteristics, adapted from [6]

level of yttria doping. Doping with yttria increases the number of oxygen vacancies, thereby increasing the diffusion constant of the oxygen within the zirconia. Due to the higher probability of hitting a Y-Y pair, which has a higher binding energy with oxygen, the average hopping energy for oxygen increases. The optimal concentration of yttria with the highest oxygen ion conductivity has been shown to be around 8.3 % (Figure 2.2) [7].

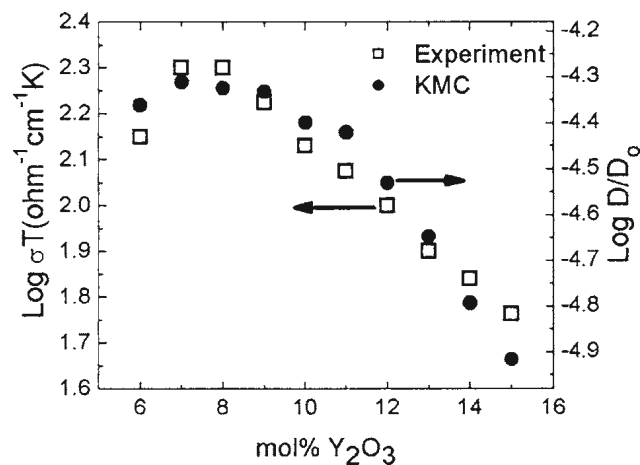


Figure 2.2: Oxygen ion conductivity and diffusion constant of zirconia with varying yttria doping, experimental values and kinetic monte carlo simulation (KMC), taken from [9]

In contrast, CGO has a higher electronic conductivity when exposed to reducing environments at elevated temperatures. This higher electronic conductivity leads

to higher leakage currents, which decrease the power output of the fuel cell. At temperatures below 500 °C, the electronic conductivity of CGO is sufficiently low to make it a promising candidate for low-temperature SOFCs. A typical doping level for CGO is around 20 wt. %.

Alternative electrolyte candidate materials include Scandia Doped Zirconia, which has a performance profile similar to that of YSZ but is more expensive, and the strontium- and magnesium- doped lanthanum gallate LaGaO_3 which has an attractive temperature range of 600 – 700 °C but suffers from phase instability, which adversely affects its long-term durability [7].

2.1.2 Electrode materials

In general, the two electrodes should conduct both ions and electrons. The anode has to be catalytically active in oxidizing the fuel, whereas the cathode has to be effective at reducing oxygen.

Anode materials

The anode of an SOFC has to be stable at relatively high operational temperatures and in reducing anode environments. It has to be catalytically active to oxidize the fuel and it should be porous, to allow for the flow of gas to and the removal of the reaction products from the electrolyte [10]. The porosity of the anode should be maintained throughout the lifetime of the fuel cell; in other words, any sintering effects of the pores should be inhibited. The choices of materials for SOFC anodes mainly comprise nickel, cobalt, and precious metals. Since cobalt and precious metals are expensive, the most commonly used anode material is nickel [8]. Nickel is usually combined with YSZ to achieve the desired mixed conduction properties. The challenge in combining nickel with YSZ is the mismatch of their thermal expansion coefficients. This problem can be resolved by incorporating nickel particles into a YSZ matrix, to form a so-called cermet. By increasing the nickel content of the cermet, the electrical conductivity and the thermal expansion coefficient are increased. The nickel content of the cermet has to be just above 30 vol. % to avoid cracking with the electrolyte, due to the increased thermal expansion coefficient, and to ensure sufficiently high electrical conductivity [8, 10].

Cathode materials

The cathode of an SOFC has to be: both ionic and electronically conductive; porous; and stable at high operational temperatures [10]. In contrast to the anode, the stability of the cathode has to be maintained in oxidizing environments. Potential cathode materials encompass a wide range of mixed oxides, since all stable (noble) metals are excluded for cost reasons. The most commonly reported cathode material is Strontium-Doped Lanthanum Magnetite (LSM) in the form of $\text{La}_{0.8}\text{Sr}_{0.2}\text{MnO}_3$ [7]. Alternative materials include doped lanthanum cobaltite (LaCoO_3) which is co-doped

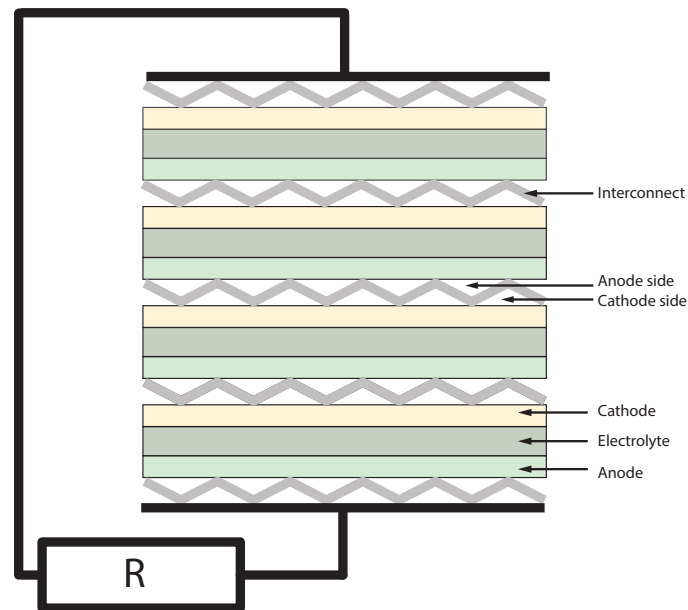


Figure 2.3: Schematic diagram of a planar SOFC stack

with strontium and iron to form $\text{La}_{1-x}\text{Sr}_x\text{Co}_{1-y}\text{Fe}_y\text{O}_3$ (LSCF). Compared to LSM, LSCF has a higher electrical conductivity but tends to react with the electrolyte, which makes it only suitable for use as a cathode at intermediate temperatures [7].

2.1.3 Interconnects

A single fuel cell element usually produces less than 1 V of electrical potential, depending on the efficiency of the fuel cell and the fuel utilization. Since a voltage output of just 1 V is rather inconvenient for most applications and for achieving a higher power density, several fuel cell elements must be combined. Therefore, planar fuel cell elements are usually placed on top of each other to form a stack. A connector is needed between each fuel cell element to join two cells electronically and to separate the cathodic atmosphere of one cell from the anodic atmosphere of the next cell. These connecting elements are called interconnects or bipolar plates (the latter term is mainly used for PEMFCs). An SOFC stack using planar fuel cell elements in combination with interconnects is shown schematically in Figure 2.3 [5, 11].

The requirements for interconnects are: a similar thermal expansion coefficient; good electrical conductivity; gas tightness; and stability at the operational temperatures of the SOFC and in the respective atmospheres [5, 11, 12]. For mass production, the interconnects need to be cost-effective. In early SOFCs, thick ceramic interconnect plates were employed that were heavy and that required extensive machining and high operational temperatures to be sufficiently conductive. Thanks to recent improvements brought about by research on electrolytes and electrodes, the operational temperatures have been lowered sufficiently to allow the utilization of metallic interconnects.

Ceramic interconnect materials

Ceramic interconnects offered the advantage of similar thermal expansion coefficient and relatively high stability, in both anodic and cathodic atmospheres. Only lanthanum chromite, doped with either CaO or SrO, meets the stringent requirements for interconnect application. Compared to metallic interconnects, lanthanum chromite is expensive and is less mechanically stable [12,13]. Moreover, the electrical and heat conductivities of p-type conducting materials are far lower than those of metallic materials [14].

Ferritic stainless steels

Ferritic stainless steels suitable for interconnect applications contain chromium at concentrations in the range of 10-26 wt. % and are relatively stable at high temperatures. The crystal structure is body-centered-cubic, and they have a matching coefficient of thermal expansion (CTE) of about $10 \times 10^{-6}/\text{K}$. For SOFCs, alloys with a chromium content in the range of 18 to 23 wt.% have shown promise. Examples of alloys that have been specially developed for an SOFC interconnect application are: Crofer 22 APU and Crofer 22 H from ThyssenKrupp VDM; Sandvik Sanergy HT from Sandvik Materials Technology; and ZMG 232 G10 from Hitachi Metals [15–17]. These alloys have been optimized with respect to corrosion protection, mechanical properties, and chromium evaporation. More detailed information about the challenges associated with metallic interconnects can be found in Section 2.3.

2.2 Corrosion of metals

Corrosion is the gradual degradation of a material (usually a metal) through reaction with its environment. In general, corrosion can be of two types: aqueous or atmospheric corrosion; and high-temperature corrosion. Aqueous corrosion occurs already at very low temperatures, and it always involves some kind of electrolyte. In contrast, high-temperature corrosion entails reactions between metals and their surrounding gas phase. For the metallic interconnects used in SOFCs, the relevant corrosion processes are limited to high-temperature corrosion, which is the focus of the following sections.

2.2.1 Thermodynamics

At high temperatures, metals can react directly with the surrounding gas phase to form products, such as oxides, carbides, nitrides, and sulfides [18]. The reaction between oxygen and a metal can be written as in Equation 2.4. It can only occur if the free enthalpy ΔG° is negative. As the reaction involves oxygen, an equilibrium oxygen partial pressure can be expressed as in Equation 2.5. If the pressure is lower than the equilibrium partial pressure, no oxide will be formed; at higher partial

pressures, the reaction is thermodynamically favored.



The term a_M describes the thermodynamic activity of the metal (it is equal to 1 for a pure metal), and $a_{M_xO_y}$ is the thermodynamic activity for the oxide in a solid solution of oxides [19].

$$p\text{O}_2 = \frac{a_{M_xO_y}^{2/y}}{a_M^{2x/y}} \exp(\Delta G^\circ / RT) \quad (2.5)$$

Ellingham/Richardson diagrams can be used to predict oxide formation for a specific metal at a specific temperature and at a specific partial oxygen pressure. This type of diagram, which was first introduced by Harold J.T. Ellingham in 1944 [20], combines the free enthalpy ΔG° with the corresponding equilibrium partial pressure of oxygen across different temperatures. More stable oxides are plotted in the lower part of the Ellingham/Richardson diagram. A simplified Ellingham/Richardson diagram is shown in Figure 2.4. It not only helps to predict whether or not a specific oxide will form of a metal, but also can be useful in predicting which oxides will form on an alloy (for a given temperature and atmosphere).

2.2.2 Kinetics

As described in the previous section, it is possible to predict whether specific oxidation reactions will be thermodynamically favored or not. The thermodynamic predictions do not give any information about the reaction rate or if an oxidation reaction will take place at all, in case the reaction rate is too slow.

The oxidation of a metal can be divided into two steps, as illustrated in Figure 2.5. There is an initial oxidation step, in which an unoxidized (blank) metal is exposed to an oxidizing atmosphere. During the first moments of exposure of the metal to high temperature and an oxidizing environment, oxygen atoms are adsorbed onto the metal surface. These oxygen atoms are reduced and begin to form oxide islands. Thereafter, these oxide islands expand until the entire surface is covered with oxide. Thus, the metal is isolated from the atmosphere by an oxide scale. For further oxidization of the metal, metal ions have to diffuse through the oxide to the outer surface or oxygen ions have to diffuse through the oxide scale to the metal interface. These two diffusion processes can occur simultaneously. Depending on the predominant diffusion process, the oxide scales can be classified as outward-growing (metal ion diffusion outward) or inward-growing (oxygen ion diffusion inward) [18].

A commonly used method to measure the corrosion rate of a metal and to predict its lifetime is to monitor the mass change of a sample over exposure time. This analysis can be performed either *in situ* during exposure with thermogravimetry or *ex situ* after varying exposure times. If no volatilization or oxide scale spallation processes are active, the mass change is equal to the sum of the oxygen uptake and metal

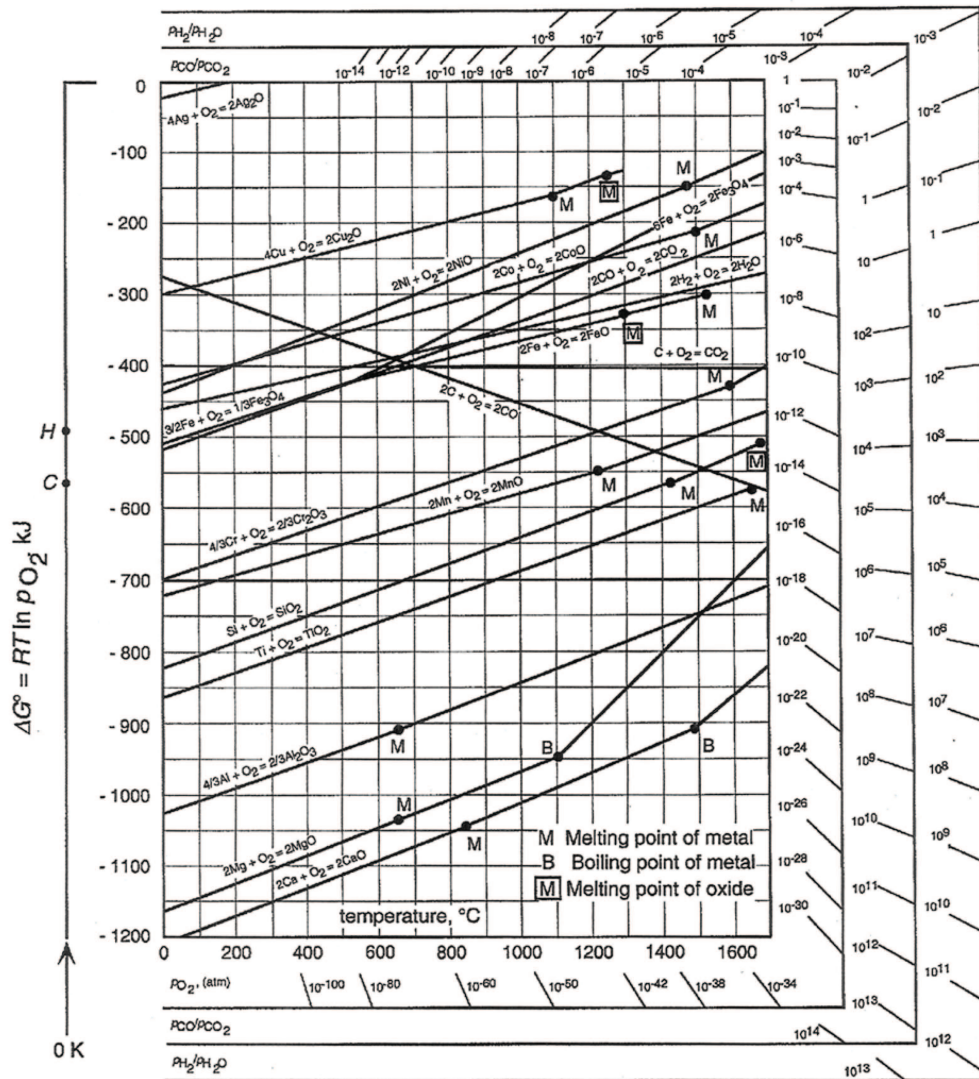


Figure 2.4: Ellingham/Richardson diagram for various metals, taken from [21]

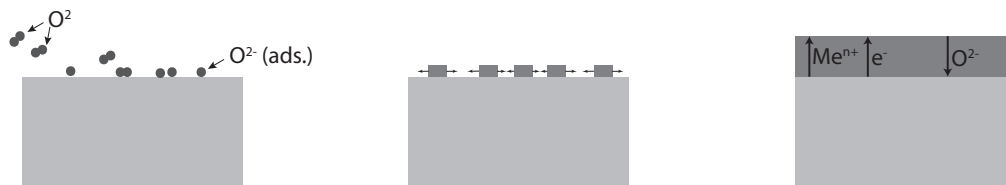


Figure 2.5: Step-wise oxide scale formation; from oxygen adsorption, oxide nucleation and oxide scale growth adapted from [18].

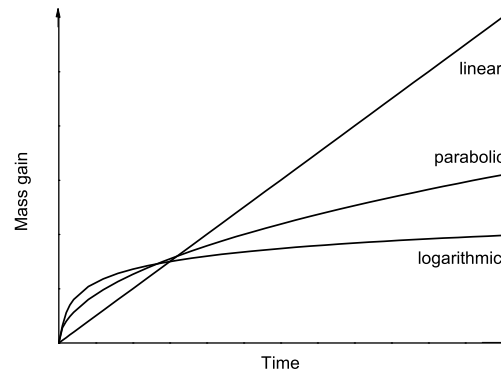


Figure 2.6: Mass gain curves for three common oxidation mechanisms, adapted from [22]

consumption. Depending on the oxidation process, one can distinguish between the different oxide scale growth mechanisms: parabolic, logarithmic, and linear (Figure 2.6).

Parabolic mechanism

A parabolic oxidation process depends on solid-state diffusion and it can be expressed using a theory introduced by C. Wagner. The model was first introduced in 1933 and is based on the following assumptions: a well-adhered oxide scale is formed; the growth rate is determined by solid-state diffusion; local equilibria exist at the metal/oxide interface and at the gas/oxide interface; and oxygen solubility in the metal is negligible [23]. Since the growth rate is only dependent upon the diffusion of ions or electrons through the oxide scale, it will decrease with time due to the increasing lengths of the diffusion paths. The thickness of the oxide scale increases parabolically with time and can be expressed using Equations 2.6 and 2.7 [18].

$$dx/dt = k'_p * 1/x \quad (2.6)$$

$$x^2 = 2k'_p t + C = k_p t + C \quad (2.7)$$

Where x is the oxide thickness, t is the time, k'_p is the parabolic rate constant and C is the integration constant. Parabolic oxidation behavior is often desirable because it is the result of a protective oxide scale.

Logarithmic mechanism

Logarithmic oxide scale growth can usually be observed at temperatures below 400°C and after rapid initial oxidation, the reaction rate drops to almost zero. There is no general consensus regarding the reaction mechanism underlying logarithmic oxidation. Proposed explanations for the rate-determining step are ion or electron transport due to an electric field, chemisorption or cavity formation within the oxide film [24].

Linear mechanism

If the mass gain curve follows a linear trend, the oxide scale has no protective properties. The rate of reaction stays constant and is independent of the amount of gas or metal consumed. This is usually the case if the rate-controlling step within the reaction is either a surface or phase boundary process [18].

Break-away corrosion

Break-away corrosion is used as a synonym for a combination of two rate equations. Break-away corrosion can happen after an initial parabolic oxidation process, which is then followed by a linear or faster parabolic oxidation process. In this case, the protective oxide scale disintegrates at some point, after which it is no longer protective. Break-down of a protective oxide scale occurs if an alloy is depleted of protective oxide-forming atoms [18].

2.3 Interconnect-related corrosion challenges

The use of ferritic stainless steels as metallic interconnects for SOFCs faces three major challenges: 1) degradation due to corrosion; 2) evaporation of chromium; and 3) increasing electrical resistance due to the growing chromia scale. Besides optimization of alloy composition, several studies have shown that additional coatings are effective in improving interconnect performance. The following sections describe the specific challenges facing interconnects and propose some solutions. Since the focus of this thesis is on the cathode side improvements, the following sections will deal with problems related to cathode side environment.

2.3.1 Corrosion

On the cathode side, the interconnect is exposed to an air atmosphere, which, owing to humidity, also contains a small amount of water. Several measures can be implemented to prevent rapid oxidation in this atmosphere. The most commonly used approach is to design alloys that form protective oxide scales that are slow growing and strongly adhere to the metal. Common examples of protective scales are alumina or chromia, and less commonly, silica-forming alloys. As mentioned above, chromia formers are the only materials considered for interconnect applications, since alumina and silica formers are, due to their high electrical resistivities, unsuitable as interconnects. As long as the steel contains sufficient amounts of chromium, the protective scale will continue to grow. When, due to the oxidation or volatilization of chromium (see section 2.3.2), the chromium content in the steel falls below a certain threshold, rapid break-away oxidation can occur. Depending on the used alloy and the experimental conditions, this threshold is reached at a chromium content of approximately 16% [25]. The problem of chromium depletion is exacerbated by using very thin interconnects, thereby reducing the chromium reservoir of the interconnect.

Another corrosion problem that is observed for interconnects is so-called spallation of the oxide scale, which can occur for various reasons, including mismatch of the thermal expansion coefficients (CTEs) between the metal and the scale, growth stresses during oxidation, and poor scale adhesion resulting in a debonding of the oxide from the metal. Some researchers have proposed subscale silica formation as the reason for oxide scale spallation, too [5, 15, 26].

Reactive Elements

In addition to designing alloys that form protective oxide scales that prevent break-away corrosion of the metal, so-called reactive elements can be added to the alloy. Reactive elements that belong to the rare earth elements, such as cerium, lanthanum, yttrium, and zirconium, are known to improve significantly the corrosion resistances of alumina- and chromia-forming alloys when added in small quantities [27]. It has been proposed that the addition of atoms with high ionic radius and high oxygen affinity is more beneficial in terms of the protection of an alloy [28]. To date, there is no clear consensus as to the mechanism underlying the reactive element effect. As exemplified by Wittle and Stringer in 1980 [28] and revised by Pint in 2003 [27], there are different suggestions as to why reactive elements enhance corrosion resistance. Several mechanisms have been proposed to explain the beneficial effects of reactive elements, including a change in the oxide growth mechanism, improvement of the chemical bonding between substrate and oxide, and a change in the oxygen vacancy diffusion (the so-called vacancy sink model).

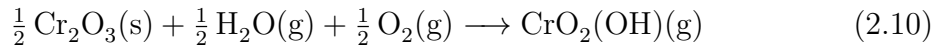
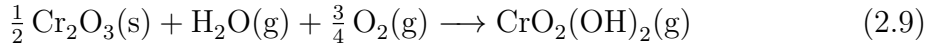
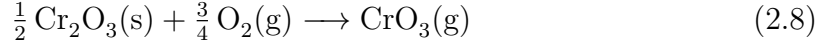
Reactive Element coatings

It has been shown that even a very thin coating of reactive elements can have the same beneficial effect on corrosion as small additions of the same reactive elements to the alloy [26, 29–32]. Fontana et al. have shown improved corrosion resistance and oxide scale adhesion for selected chromia-forming alloys, such as Crofer 22 APU, AL452, and Haynes 230, with RE coatings of neodymium, lanthanum or yttrium oxides [29]. Alman and colleagues have reported a slower oxidation rate and improved scale adhesion for cerium-coated Crofer 22 APU [26].

2.3.2 Chromium evaporation

Chromium oxide is thermodynamically unstable under humid conditions at high temperatures, and this leads to the evaporation of volatile chromic species. It has been shown that different volatile species are involved in the degradation process, including CrO_3 , $\text{CrO}_2(\text{OH})_2$ and $\text{CrO}_2(\text{OH})$. The following reactions are involved to form these species, see Equations 2.8 - 2.10. Ebbinghaus et al. [33, 34] have proposed that the predominant reaction involved in chromium evaporation is 2.9. This is valid for temperatures below 1800 °C and in atmospheres containing oxygen and water vapor. Opila et al revised this to temperatures up to 900 °C [35, 36]. Chromium evaporation

is influenced by various factors, such as temperature, water vapor content, and oxygen pressure. In an SOFC application in which high flow rates are applied, chromium evaporation can even be increased, since the constant gas exchange prevents the attainment of a chromium-saturated gas phase, so equilibrium is not reached.



Coatings for preventing Chromium evaporation

Various coatings have been reported to be effective in decreasing or preventing the volatilization of chromium. In general, these coatings can be classified as perovskite structures and spinel structures. Examples of perovskite coatings are LSC (LaScCrO_3), LSM (LaSrMnO_3) or LSCF (LaSrCoFeO_3), which usually have to be applied in thick layers and often suffer from poor adhesion to the substrate [37–40]. Spinel coatings, which are mostly based on cobalt, are often used in combination with other transition metals to obtain a cobalt-manganese top oxide. Cobalt-containing spinel coatings decrease the evaporation of chromium by a factor of 10 [41]. Extensive research has been conducted on different thin film coating technologies for applying spinel coatings. These can be differentiated into conversion coatings (coatings applied as metals) and oxide coatings (coatings that are already deposited as spinel oxides). The advantage of conversion coatings is that they can be applied in a very thin layer and can be deformed without detaching from the substrate [42]. Most spinel coatings show good electrical conductivities, see also section 2.3.3 [43].

2.3.3 Electrical conduction of oxide scales

Good electrical conduction between the stacked fuel cell elements is one of the key desirable features of an interconnect. The main challenge with respect to the conductivity of an interconnect is the growing oxide scale, which has far lower electrical conductivity than the underlying steel. Therefore, it is most important to focus on the oxide scale to improve the electronic properties of the interconnect [31].

Generally the conduction of any material can be described using the Formula 2.11.

$$\sigma = \sum \mu_i * n_i * q_i \quad (2.11)$$

$$\sigma = \sigma_0 * e^{\frac{-E_a}{R*T}} \quad (2.12)$$

Where μ_i is the mobility of charge carrier i , n_i is the number of charge carrier i and q_i is the charge of charge carrier i . Different types of charge carriers come into account for oxides, such as electrons, electron holes, ions or ion holes. Increasing temperature affects the mobility μ_i of electrons usually negatively and ions positive, whereas the charge carrier concentration n_i increases with higher temperature. Oxides usually show an increase in conductivity at higher temperatures due to the fact that the generation of more charge carriers compensates for the decreased electron mobility. This is in contrast to metals in which the decreased electron mobility μ_i outweighs the increased charge carrier generation. The temperature dependence of the conductivity of oxide scales can also be expressed using the Arrhenius relation, (see Equation 2.12). Where σ_0 is a pre-exponential factor, R the universal gas constant, T the absolute temperature and E_a the activation energy. The activation energy is, in addition to the total conductivity, an important material property for identifying which phases of a microstructure contribute most to conduction [44]

Electric properties of chromia

Since only chromia-forming alloys are taken into consideration for an interconnect application, the electrical properties of the interconnect are strongly influenced by the growing chromia scale. At high temperatures, chromia is an intrinsic semiconducting material with a band gap energy of approximately 2.7 to 3.3 eV, whereas at lower temperatures it becomes an extrinsic semiconducting material [45–49]. While there is no agreement as to the exact temperature at which the transition from extrinsic to intrinsic semiconducting occurs, most publications report this temperature to lie within the range of 900 to 1200 °C. In Figure 2.7 conductivity values for chromia at high oxygen partial pressures ($> 10^{-2}$ bar) are summarized [45, 46, 48, 50–57]. It is evident that while there is fairly good agreement within the intrinsic semiconducting region (high temperatures), there is a significant spread in the conductivity values within the extrinsic semiconducting region (lower temperatures). There is good agreement with regard to activation energy for the intrinsic region, whereas the extrinsic region shows differences in shape, slope, and absolute conductivity level. In some of the plotted references there is an indication of a transition zone, where the conductivity stays constant with temperature, just before the intrinsic region is reached. The differences are considered to be caused by differences in purity levels, densities or grain boundary concentrations [45, 46, 51]. Moreover there still is no agreement on the exact mechanism for the electrical conduction of chromia at low temperatures. At temperatures below 1000 °C pure chromia is known to be a mostly p-type conducting material and the conductivity of chromia is slightly dependent upon the partial pressure of oxygen [45]. There is agreement on the fact that chromia at low temperatures is metal-deficient and that its conductivity reflects that deficiency. Lebreau et al. used computational methods to investigate the electronic, transport, and defective properties of chromia and revealed that the most stable defects are chromium Frenkel defects and chromium vacancy defects, both of which add energy levels within the

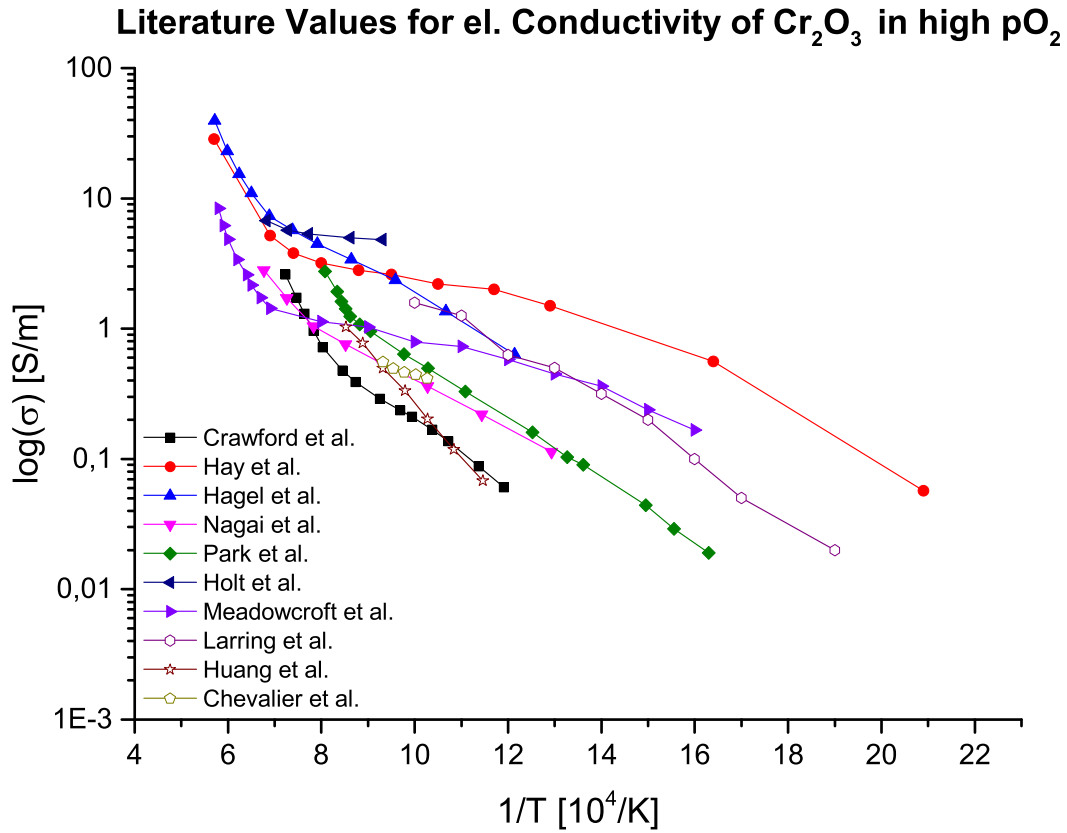


Figure 2.7: Electrical conductivity of chromia, reported by different authors [45, 46, 48, 50–57].

band gap [47]. Meadowcroft et al. have claimed that the low-temperature conductivity of chromia is dependent mainly upon the thermal history, and that defects are "frozen-in" when chromia is cooled from higher temperatures [46]. However, experimental proof for this assertion is lacking. Holt and Kofstad observed very long equilibrium times for conductivity when chromia was exposed to different atmospheres, and they observed substantial hysteresis effects when chromia was measured at different temperatures [45]. Larring and coworkers observed a dependency pattern of the electronic conductivity of chromia oxide scales grown at different humidity levels, although they could not exclude the effects of different oxide morphologies when the samples were exposed to different humidity levels [55]. In terms of interconnect research, it is still not clear which activation energy is relevant for electrical conduction and if it is possible to translate directly the conductivity values obtained for bulk samples to chromia oxide scales.

Electric properties of spinels

The most commonly suggested alloys for an SOFC interconnect application are those designed to form a chromium manganese spinel as the outer oxide layer. The electrical conductivity and also the activation energy of a chromium manganese spinel decreases as the manganese content increases [58]. If the ratio of manganese to chromium is greater than 1:1, meaning there is more manganese than chromium in the spinel, the conductivity at the typical operational temperatures of SOFCs is less than that of chromia [31].

As described in the previous section 2.3.2, additional coatings for decreasing the evaporation of chromium are inevitable. The most promising coatings for reducing chromium evaporation are cobalt spinel coatings, although others, such as copper spinel coatings, have also been considered. Since all barrier coatings are oxidized before, or during the very first moments of exposure, it is essential that they are good conductors. Petric et al. conducted an extensive study of the conductivities of different spinels [43]. Table 2.2 lists conductivities and the coefficients of thermal expansion at 800 °C (except where noted) of different transition metal spinels [43]. Petric et al. concluded that spinels formed from cobalt and manganese, copper and manganese, and copper and iron are, from the conductivity and thermal expansion points of view, the most promising candidates for interconnect coatings [43].

	Mg	Mn	Co	Ni	Cu	Zn
Al	MgAl ₂ O ₄ $\sigma = 10^{-6}$ $\alpha = 9.0$	MnAl ₂ O ₄ $\sigma = 10^{-3}$ $\alpha = 7.9$	CoAl ₂ O ₄ $\sigma = 10^{-5}$ $\alpha = 8.7$	NiAl ₂ O ₄ $\sigma = 10^{-4}$ $\alpha = 8.1$	CuAl ₂ O ₄ $\sigma = 0.05$ $\alpha = -$	ZnAl ₂ O ₄ $\sigma = 10^{-6}$ $\alpha = 8.7$
Cr	MgCr ₂ O ₄ $\sigma = 0.02$ $\alpha = 7.2$	Mn _{1.2} Cr _{1.8} O ₄ $\sigma = 0.02$ $\alpha = 6.8$	CoCr ₂ O ₄ $\sigma = 7.4$ $\alpha = 7.5$	NiCr ₂ O ₄ $\sigma = 0.73$ $\alpha = 7.3$	CuCr ₂ O ₄ $\sigma = 0.40$ $\alpha = -$	ZnCr ₂ O ₄ $\sigma = 0.01$ $\alpha = 7.1$
Mn	MgMn ₂ O ₄ $\sigma = 0.97$ $\alpha = 8.7$	Mn ₃ O ₄ $\sigma = 0.10$ $\alpha = 8.8$	CoMn ₂ O ₄ $\sigma = 6.4$ $\alpha = 7.0$	NiMn ₂ O ₄ $\sigma = 1.4$ $\alpha = 8.5$	Cu _{1.3} Mn _{1.7} O ₄ $\sigma = 225$ (750 °C) $\alpha = 12.2$	ZnMn ₂ O ₄
Fe	MgFe ₂ O ₄ $\sigma = 0.08$ $\alpha = 12.3$	MnFe ₂ O ₄ $\sigma = 8.0$ $\alpha = 12.5$	CoFe ₂ O ₄ $\sigma = 0.93$ $\alpha = 12.1$	NiFe ₂ O ₄ $\sigma = 0.26$ $\alpha = 10.8$	CuFe ₂ O ₄ $\sigma = 9.1$ $\alpha = 11.2$	ZnFe ₂ O ₄ $\sigma = 0.07$ $\alpha = 7.0$
Co		MnCo ₂ O ₄ $\sigma = 60$ $\alpha = 9.7$	Co ₃ O ₄ $\sigma = 6.7$ $\alpha = 9.3$			

Table 2.2: Specific conductivities σ (given in S/cm) and thermal expansion coefficients α (given in ppm/K) of different spinels at 800 °C, except where noted, taken from [43]

CHAPTER 3

Materials and Methods

3.1 Investigated materials

During the work of this thesis, the following stainless steels were investigated: AISI 441, Sanergy HT, and Crofer APU. Their compositions are listed in Table 3.1. AISI 441 is a ferritic stainless steel that was developed for high-temperature applications, although it was not specially designed for an SOFC application. In contrast, Sanergy HT and Crofer APU are ferritic stainless steels that were optimized for the use as interconnect materials.

		Fe	Cr	C	Si	Mn	Nb	Ti	P	Ni	Mo	Cu	RE
AISI 441	wt.%	bal.	17.83	0.012	0.55	0.26	0.48	0.14	0.024	0.13			no
Sandvik Sanergy HT	wt.%	bal.	22.4	0.01	0.07	0.25	0.4	0.06	0.13	0.8	0.9	0.017	0.06 (Zr)
Crofer APU	wt.%	bal.	22.79	0.004	0.02	0.41	0.01	0.06	0.003	0.02	0.01	0.01	0.1 (La)

Table 3.1: Materials composition, values given from manufacturer.

AISI 441 and Sanergy HT were investigated uncoated and coated with different coatings. The coatings tested on AISI 441 are shown in Table 3.2 and the ones tested on Sanergy HT are shown in Table 3.3. On AISI 441 two reactive element coatings, one of cerium and one of lanthanum and two combinatorial coatings of cerium and cobalt and lanthanum and cobalt were tested. Sanergy HT was exposed with coatings of cobalt, cerium with cobalt, copper with manganese and copper with iron, as shown in Table 3.3. Crofer APU was investigated as reference material for the ASR characterization only.

Sample designation	Inner coating	Outer coating
Uncoated		
Ce coated	10 nm cerium	-
La coated	10 nm lanthanum	-
Ce/Co coated	10 nm cerium	630 nm cobalt
La/Co coated	10 nm lanthanum	630 nm cobalt

Table 3.2: Investigated coating systems on AISI 441.

Sample designation	Inner coating	Outer coating
Co	-	630 nm cobalt
Ce/Co	10 nm cerium	630 nm cobalt
Mn/Cu	830 nm manganese	400 nm copper
Fe/Cu	800 nm iron	400 nm copper
Cu/Fe*	400 nm copper	800 nm iron

Table 3.3: Investigated coating systems on Sanergy HT. *A 50 nm thick Fe strike coating was applied prior to the copper coating.

3.2 Sample preparation

All the investigated materials were obtained as sheets of 0.2 mm thickness from Sandvik Materials Technology AB, with the exception of Crofer APU, which was purchased from ThyssenKrupp at a sheet thickness of 0.5 mm. The coatings were prepared using an industrially available physical vapor deposition process conducted by Sandvik Material Technology AB. The received sheets were cut into sections of 15 x 15 mm² using either scissors or a metal-cutting tool. Thereafter, a cleaning procedure, first in acetone and then in ethanol with the application of ultrasound, was performed. The samples were subsequently weighed using either a Satorius MC 5 or a Mettler Toledo XP6 microbalance.

3.3 Exposure

Tubular furnaces were used to expose the samples to an SOFC cathode-side environment. A schematic of the experimental setup is shown in Figure 3.1. The gas flow was set to a value at 6000 ml/min, and the gas was humidified using a heated water wash bulb in combination with a spiral cooler. The spiral cooler was set to

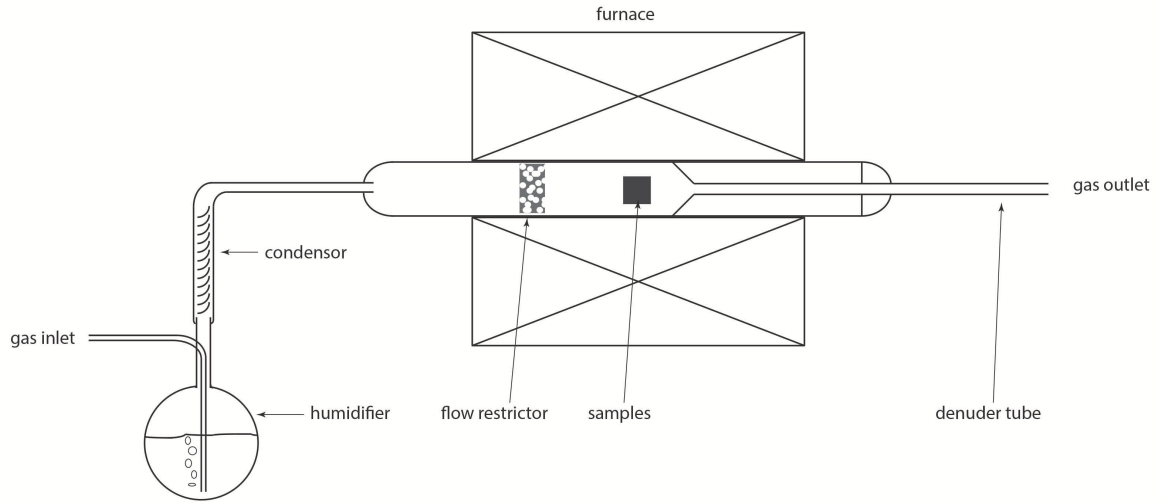


Figure 3.1: Scheme of experimental setup.

a dew-point of 24.4°C to ensure a water content of 3 %. When measuring the mass gain or for pre-oxidation of samples for the ASR measurement, up to six samples were exposed in one run. Only three samples were exposed simultaneously for chromium evaporation measurements. The evaporation of chromium was measured using the denuder technique.

3.3.1 Denuder technique

In this study, the denuder technique, which was developed at Chalmers University of Technology, was used to quantify the amount of volatilized chromium. The technique utilizes a tubular furnace setup, as shown in Figure 3.1. The outlet of the furnace is equipped with a so-called denuder tube. The exhaust gas is led through this denuder tube, which is coated on its inside walls with sodium carbonate. The sodium carbonate reacts with the evaporated chromium species, as shown in Equation 3.1.



The denuder tubes can then be changed at regular time intervals, allowing time-resolved measurements of chromium evaporation. The removed denuder tubes were leached out with Milli-Q water. The wash-out solutions were then quantified for chromium concentration using a photo spectroscope. The concentration dependency of the absorption was calibrated using potassium dichromate solutions at different concentrations. The absorption was measured between 0.05 and 2.1 a.u. and showed a linear dependency on the chromium concentration (see Figure 3.2). All the chromium evaporation experiments were conducted in such a way as to maintain the measured concentrations between the calibrated values. The absorption factor was calculated as 0.04043 based on the chromate concentration [ppm].

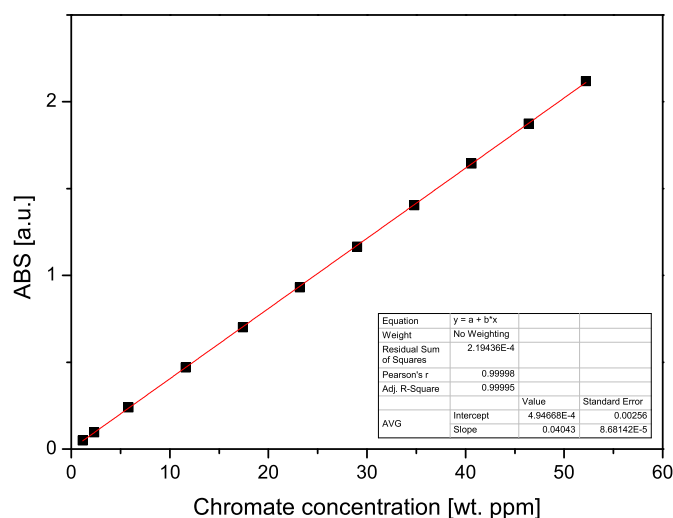


Figure 3.2: Linear dependency of concentration and absorption.

3.4 Analytical techniques

The samples were post-analyzed mainly using Scanning Electron Microscopy (SEM), although Energy Dispersive X-ray analysis (EDX), X-ray Diffractometry (XRD), and electrical characterizations were carried out for selected samples.

3.4.1 Scanning electron microscopy

In an SEM, a focused electron beam is scanned over the surface of the sample. By interacting with the atoms of the sample, different emissions are excited. These emissions include secondary electrons, back-scattered electrons, auger electrons, and X-ray emissions, see Figure 3.3. Depending on the detector used, these emissions can be transformed into a signal that is then used to create a digital image of the sample [24]. For the work of this thesis, mainly secondary and back-scattered electrons were used to image the investigated samples. X-ray emissions were used to determine the composition of the sample. Depending on the signal used, a different interaction volume has to be taken into account. A scheme for the interaction volume is shown in Figure 3.4 [22, 59].

Secondary electrons

Secondary electrons (SE) are generated when an incoming electron within the electron beam interacts with the electrons of an atom in the sample. The incoming electron is scattered in the electron shell and the released energy is compensated for by releasing a second electron. These electrons usually have energies of below 50 eV, which is a

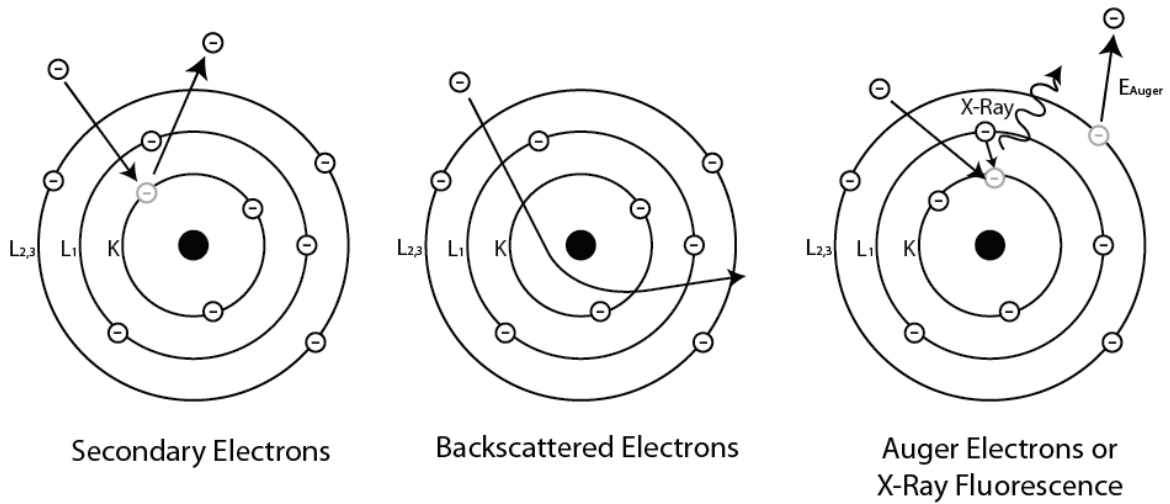


Figure 3.3: Electron atom interactions taken from [60].

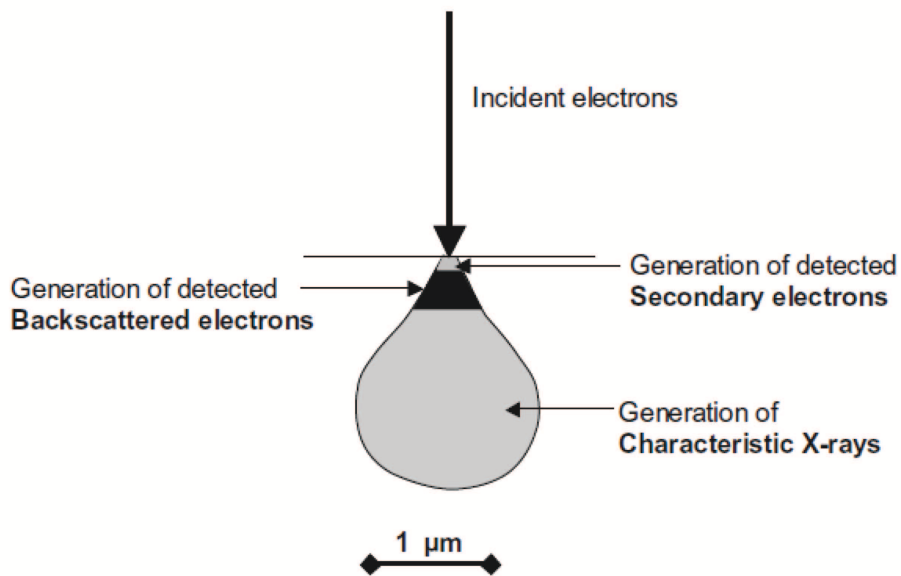


Figure 3.4: Interaction volume of incoming electron beam with sample volume [61].

rather low level. As shown in Figure 3.4, secondary electrons are relatively surface-sensitive and can be used for imaging surface topography [22, 59].

Back-scattered electrons

Back-scattered electrons are produced when an incoming electron is elastically scattered at an atom core. They are highly energetic, with energies up to the accelerating voltage of the incoming electron beam, which increases the interaction volume, as compared to secondary electrons. Due to the higher interaction volume, the resolution and the topographic contrast decrease. A higher atomic number results in more effective back-scattering, leading to a compositional contrast, which cannot be observed using secondary electrons [22, 59].

Energy dispersive X-Ray analysis

The interactions between the incoming electrons and the electron shell of an atom lead to the emission of characteristic X-rays. This process occurs when an electron of the inner atom shell is emitted, an electron of the outer electron shell fills the vacant space, and the energy difference is compensated for by X-ray emission. Due to the specific energies linked with the different shells, only X-rays with specific energies are generated. These specific energies can be used to determine the composition of the sample [22, 59].

Focused Ion Beam milling

A Focused Ion Beam (FIB) system works in a similar way to a SEM but instead of electrons, ions are used, usually gallium ions. In contrast to electrons, these ions can be used to erode and deposit materials, as well as for imaging purposes. Machines with combined SEM and FIB allow the preparation of very fine and clean samples for SEM or Transmission Electron Microscopy (TEM) analysis [22, 59].

3.4.2 X-ray diffraction

X-ray diffraction is an analytical technique that allows examinations of the crystallographic structure of a sample. Since X-rays interact with the electron shell of an atom, diffraction can occur. The diffraction of X-rays by an atom is dependent upon the electronic structure of the atom and the energy of the incoming X-ray. X-rays are usually diffracted in all directions. However, if many atoms are aligned in an ordered structure, as in a crystal, interference effects are noted. This effect is described by Bragg's law, as depicted in Equation 3.2.

$$n * \lambda = 2d\sin(\Theta) \quad (3.2)$$

Where n is an integer, λ the wavelength of the incoming X-rays, d the distance between lattice planes and Θ the angle of incidence. If λ and Θ are known one can

calculate the distance between the lattice planes and by the use of simulations or databases also the crystal system [62].

For XRD, many measurement geometries and setups are known. In the present work, two measurement geometries have been used: grazing incidence XRD; and XRD with a Bragg-Brentano geometry (see Figures 3.5 and 3.6). Grazing incidence geometry (Siemens D5000) was used for oxide scales on metal surfaces and a Bragg-Brentano setup (Bruker D8 Advanced) was used for powder samples [62].

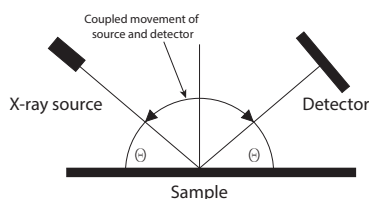


Figure 3.5: Bragg-Brentano geometry.

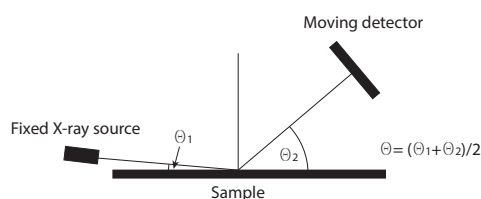


Figure 3.6: Grazing incidence geometry.

3.4.3 Electrical Characterization

Different methods have been tested for electrical characterization. The major challenge associated with measuring the electrical resistance of an oxidizing steel foil is the preparation of suitable electrodes. The most effective solution proved to be electrodes made of sputtered platinum with a painted platinum coating on top of the electrode. The electrode preparation procedure is shown in Figure 3.7. A sputter mask of 10 x 10 mm² was placed on a preoxidized sample, and the sample was then sputtered with platinum for 10 min using a Quorum 150 sputter coater and a sputter current of 60 mA, resulting in an approximately 100 nm thick platinum layer. The procedure was then repeated for the other side of the sample. After sputtering, the electrodes were re-painted with platinum paste (Metalor 6082 or Metalor 6926) using a fine brush. To remove the binder from the platinum paint, the samples were fired at 850°C in air with a peak time of 10 min.

A Probostat (NorECs, Norway) test cell, placed in a tubular furnace, was used to connect the sample to the electrical equipment. The sample was measured in a direct current (DC), alternating current (AC) or quasi-direct current, entailing AC at very low frequencies. For DC measurements, two setups were used: a Keithley 2440 current source in connection with a Keithley 2701 digital multimeter; or a Keithley 2400 in four-point resistance mode. Different currents were used depending on the resistance of the sample. Metallic samples were usually measured at a current density of 100 mA and bulk oxide samples were assessed at 1 mA, although other current densities were also tested. The samples were measured at different temperatures to allow activation energy calculations and to ensure that the oxide scale was not short circuited. A Solartron 1260A impedance analyzer was used for the AC measurements and the quasi-DC measurements. When AC characterizations were carried out a

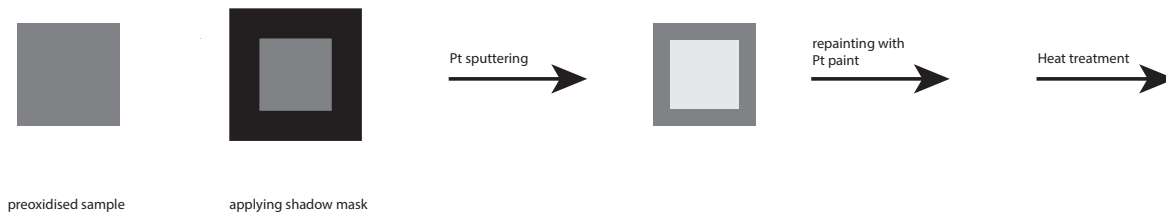


Figure 3.7: Scheme for electrode preparation.

measurement voltage of 100 mV without bias was applied to measure the impedance in the frequency range of 10 mHz to 6 MHz. The impedance was measured in 10°C steps in a temperature range from 200°C to 50°C. For quasi-DC measurements, the impedance analyzer was run at a frequency of 1 Hz, and each temperature was measured several times. Since the frequency was relatively low, the measurement was considered to be free from capacitive or inductive influences.

Results and Discussion

4.1 Corrosion and chromium evaporation

The first part of this thesis focuses on the corrosion and chromium evaporation properties of selected substrate coating combinations. The aim is to develop cost-effective solutions for interconnects that have adequate corrosion profiles and low levels of chromium evaporation. The study was conducted using two different strategies: 1) the use of a cheaper ferritic stainless steel with high-performance coatings; and 2) the use of new types of coatings applied to high-performance stainless steel.

4.1.1 Chromium evaporation measurement validation

The levels of chromium evaporation of the investigated substrate/coating combinations were measured using the denuder technique. This unique technique allows time-resolved measurements of the volatilization of chromium [63]. To assess the reproducibility of the denuder technique, uncoated stainless steel AISI 441 was exposed in different furnaces and under the same conditions of 850 °C in 3 % water containing air, which is plotted in Figure 4.1. Chromium evaporation was measured for almost 1200 h; over the entire exposure period it followed a linear trend. Two parallel exposures were carried out in different furnaces, and after a total exposure time of about 1125 h the two runs deviated by less than 1 %. In the case of problems with denuder handling or when the samples were not positioned correctly in the furnace, deviations of the chromium evaporation levels were observed. Therefore, it was concluded that the method for measuring chromium evaporation was reliable as long as the samples were standing correctly in the holder and no handling errors were made. To ensure good reliability, all subsequent experiments were performed at least twice, and whenever experimental problems were encountered the experiments were redone.

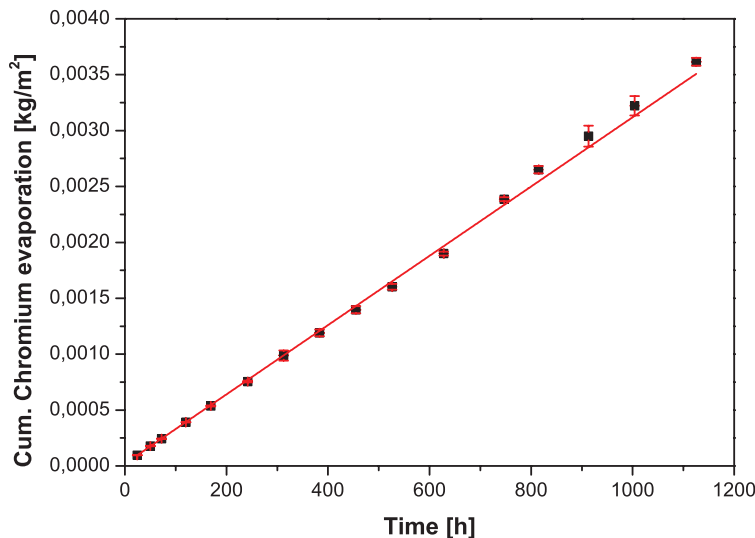


Figure 4.1: Chromium evaporation of uncoated AISI 441.

4.1.2 AISI 441 with different coatings

The first investigation used ferritic stainless steel AISI 441 that was coated with different nano-coatings. AISI 441 was chosen as the substrate material because it can be purchased at a fraction of the price of comparable SOFC interconnect-optimized ferritic steels. The investigated coatings had been previously shown by the research group of the HTC to be effective on Sanergy HT [42, 64, 65].

Gravimetric measurements and chromium evaporation

Both isothermal and discontinuous exposures were performed to monitor mass gain and chromium evaporation. The mass gains that were obtained by discontinuous exposures are plotted in Figure 4.2. After about 100 h of exposure, the uncoated material started to suffer from spallation and after exposure for 570 h a mass gain of 0.48 mg/cm² was observed. The cerium-coated material exhibited a mass gain of about 0.45 mg/cm² and the lanthanum-coated material had a mass gain of about 0.52 mg/cm² after a total exposure time of 570 h. The cerium/cobalt-coated material had a mass gain of 0.59 mg/cm² and the lanthanum/cobalt-coated material had a mass gain of 0.58 mg/cm² after the same exposure time. Both of the RE/cobalt-coated samples showed a mass gain of about 0.21 mg/cm² after only 100 min of exposure, which was attributed to the rapid oxidation of the cobalt top coating. All the coated samples exhibited an almost parabolic corrosion behavior after an initial oxidation period of 100 min. The mass gains of the coated samples exposed discontinuously did not differ significantly from those of the isothermally exposed samples. It was observed that the lanthanum/cobalt-coated samples became slightly bent after exposure. In contrast to the discontinuous gravimetric exposures, chromium evaporation was measured isothermally. The cumulative chromium evaporation over time

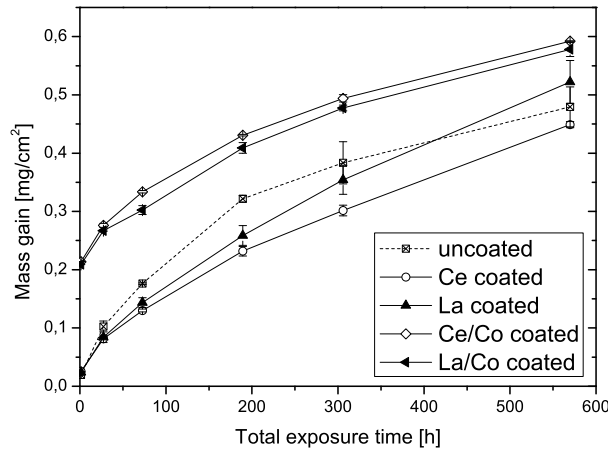


Figure 4.2: Mass gain of stainless steel 441 with different coatings.

is plotted in Figure 4.3. The uncoated material, as well as the lanthanum-coated material exhibited similar levels of chromium evaporation. The uncoated material evaporated a total mass of about 0.0014 kg/m^2 of chromium after 526 h of exposure. The lanthanum-coated material evaporated 0.0012 kg/m^2 chromium after 475 h of exposure time. The cerium-coated material evaporated 0.0015 kg/m^2 chromium during 500 h, which is about 10 % higher than the values for the uncoated and lanthanum-coated materials. The cerium/cobalt-coated material showed an approximately 90 % lower level of chromium evaporation at 0.00014 kg/m^2 . The lanthanum/cobalt-coated material evaporated also approximately 90 % less chromium than the uncoated material, with about 0.00019 kg/m^2 being evaporated after about 500 h of exposure. The levels of chromium evaporation, as shown in Figure 4.3, followed almost a linear trend. A slight decrease in the evaporation rate was seen after the first few measurements, which might be due to an initial oxidation step towards a double-layered oxide scale and until a continuous outer manganese spinel oxide layer had formed. Comparing the levels of chromium volatilization for the cerium-coated and lanthanum-coated materials, the observed 10 % increase in chromium evaporation suggested that chromium evaporation was increased by cerium. This is attributable to either a catalytic effect of cerium, due to its different oxidation states, or since it is known to suppress outward metal ion diffusion, resulting in a thinner outer oxide layer. The latter notion appears to be supported by the microstructural observations 4.1.2. The RE/cobalt-coated samples also showed a linear trend with respect to chromium evaporation. The very rapid initial oxidation of the cobalt top coating to Co_3O_4 led to immediate protection against chromium evaporation and acted as a cap layer. The outward diffusion of manganese might improve retention even further. Mass gain is one of the main indicators of the lifetime of an oxidizing steel. In the present investigation, two complications appeared when comparing the different coating systems: 1) the continuous

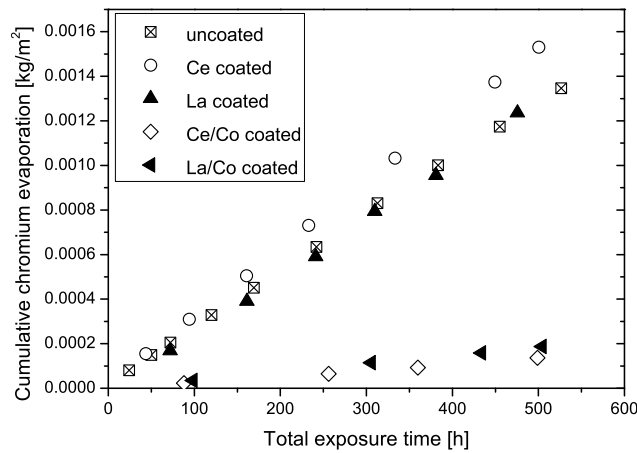


Figure 4.3: Chromium evaporation of stainless steel 441 with different coatings.

evaporation of chromium led to a mass loss; and 2) in the case of the cobalt top coatings, an initial mass gain was noted. Therefore, the mass gain data were combined with the chromium evaporation data to allow accurate comparisons of the different coating systems. The evaporated chromium was added to the mass gain by assuming that every mg of lost chromium is equivalent to 1.46 mg of Cr_2O_3 in the oxide scale. Furthermore, the initial oxidation of the cobalt top coating was subtracted from the cobalt-coated samples, by calculating the theoretical mass gain for a 630 nm-thick cobalt coating oxidized to Co_3O_4 , which is equal to 0.202 mg/cm². The aim here was to obtain a clearer picture of the influences of the different coatings on the corrosion properties of the steel. The recalculated mass gain is plotted in Figure 4.4. Due to the extensive spallation observed for the uncoated material and the consequently large difference between isothermal and discontinuous exposure, the uncoated material was excluded from the plot. The updated plot clearly shows not only the beneficial effects of the reactive element coatings, but also the positive effect that the cobalt top coating has on corrosion performance. The largest compensated mass gain was obtained with the lanthanum-coated samples, whereas the cerium-coated material oxidized slightly more slowly. The most distinctive aspect of this plot is the positive influence of the cobalt top coating. In previous studies using Sandviks Sanergy HT, only a negligible effect of the cobalt top coating on the oxidation properties was observed [64]. In contrast, Yang et al. reported a beneficial effect of a $\text{Mn}_{1.5}\text{Co}_{1.5}\text{O}_4$ coating on AISI 441, which they interpreted as being the result of limited oxygen inward diffusion, a notion that may be supported by the present work [66].

Microstructural evolution

Several SEM analyses were performed on the exposed samples, in order to obtain a better understanding of the underlying oxidation processes. A top-view image of

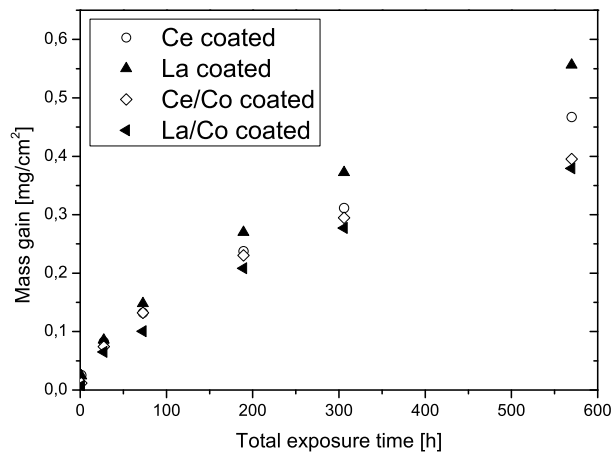


Figure 4.4: Compensated mass gain of stainless steel 441 with different coatings.

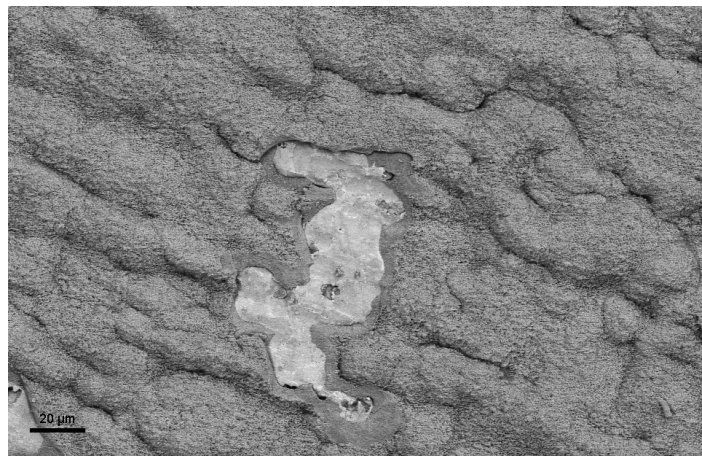


Figure 4.5: Topview of an uncoated sample exposed for 500 h.

an uncoated sample is depicted in Figure 4.5. The surface of the uncoated material appeared relatively buckled, with a linear texture, and spallation was observed at several locations. The spallation, which was also evident upon visual inspection, occurred at exposure times longer than 100 h. A cross-section of the same material (Figure 4.6), showed a double-layered oxide, with a relatively thin (approx. $0.8 \mu\text{m}$) outer oxide and thicker (approx $3.6 \mu\text{m}$ thickness) inner oxide. EDX analysis (Figure 4.7) revealed the presence of an outer manganese-rich oxide with a chromium-rich inner oxide. A zone of internal titanium-rich oxide was observed beneath the double layer oxide. In addition, some Laves phases were located in the grain boundaries, mainly containing niobium and silicon.

The level of spallation observed during the present study was relatively high compared to similar studies reported in the literature. Liu et al. reported a low level

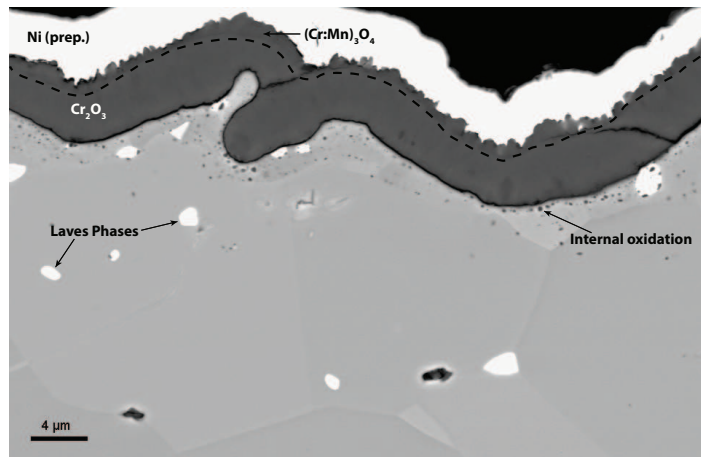


Figure 4.6: Cross-section of an uncoated sample exposed for 500 h.

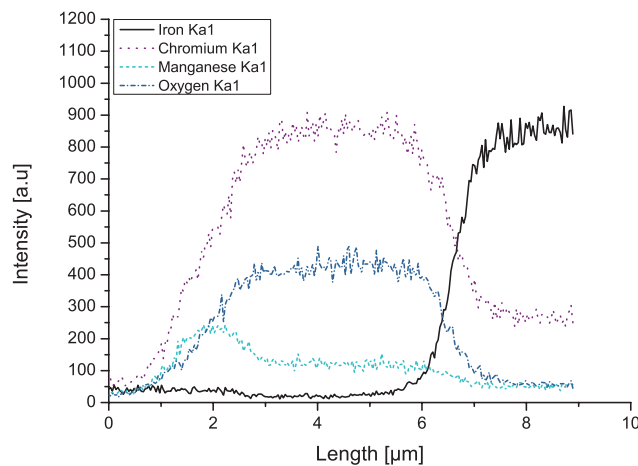


Figure 4.7: EDX line scan of an uncoated sample cross-section exposed for 500 h.

of spallation for uncoated AISI 441 exposed to stagnant air; however, it is not clear whether their investigated steel had a different chemical composition or the thermal stresses were lower due to their experimental conditions [67]. The observations of Yang et al. [63] that spallation occurs to a lesser extent and at longer exposure times are in line with those of Liu and coworkers [66]. It is possible that the observation of Yang and coworkers is the result of using a lower exposure temperature of about 800 °C. A commonly proposed explanation for oxide scale spallation in this context is sub-scale silica formation [5]. This was initially supported by the observations of Jablonski et al., who concluded that niobium content, as well as high exposure temperatures do not allow for the complete capture of the silicon contained in the steel [15]. Moreover, the investigated batch of AISI 441 contained a relatively high content of silicon (0.55 wt.% compared to 0.33 wt.% in Jablonski's investigation). In contrast to the uncoated samples, no spallation was observed on the cerium- and the lanthanum-coated materials (Figures 4.8 and 4.11). Nevertheless, a linear texture

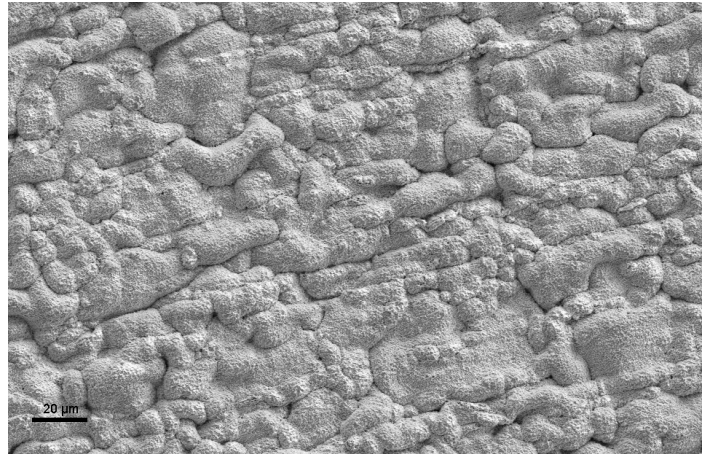


Figure 4.8: Topview of a cerium-coated sample exposed for 500 h.

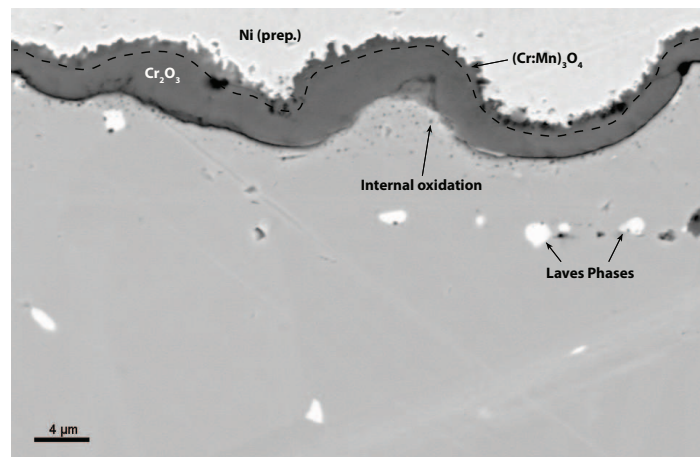


Figure 4.9: Cross-section of a cerium-coated sample exposed for 500 h.

was clearly visible within the buckling. The cross-section of a cerium-coated sample confirmed, once again, a double-layered oxide (see Figure 4.9), although the layers were slightly thinner (outer oxide approx. $0.5 \mu\text{m}$ and inner oxide approx. $2.3 \mu\text{m}$). The results of the EDX analysis of the coated samples were not significantly different from those of the uncoated material, as shown in Figure 4.10. Once again, a zone of internal oxidation with titanium oxides and niobium and silicon-rich Laves phases were observed.

A structure similar to that seen for the cerium-coated material was observed in the cross-section of the lanthanum-coated material (Figure 4.12). The thicknesses of the two oxide layers were $0.8 \mu\text{m}$ for the outer and $2.1 \mu\text{m}$ for the inner layer, i.e., within a comparable range. The EDX analysis did not reveal any major differences between the lanthanum and uncoated materials (4.13).

To investigate whether or not subscale silica formation caused the severe spallation

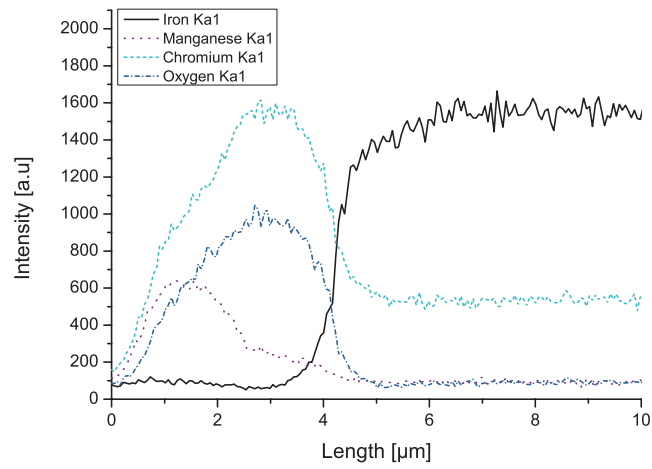


Figure 4.10: EDX line scan of a cerium-coated sample cross-section exposed for 500 h.

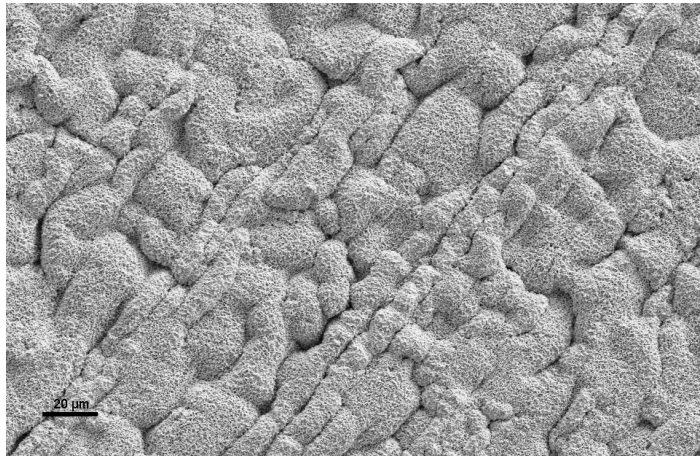


Figure 4.11: Topview of a lanthanum-coated sample exposed for 500 h.

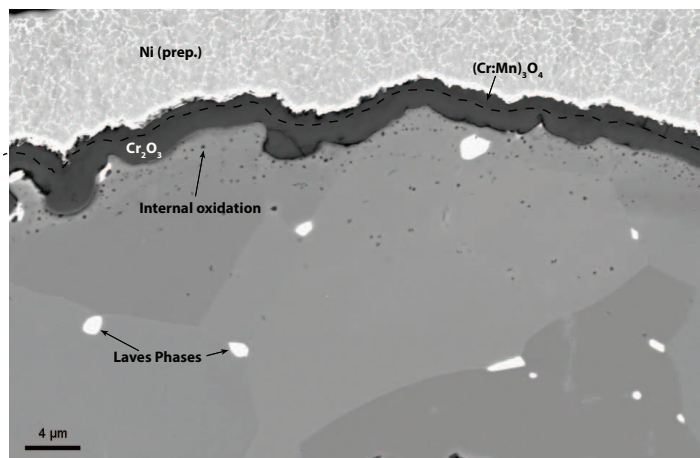


Figure 4.12: Cross-section of a lanthanum-coated sample exposed for 500 h.

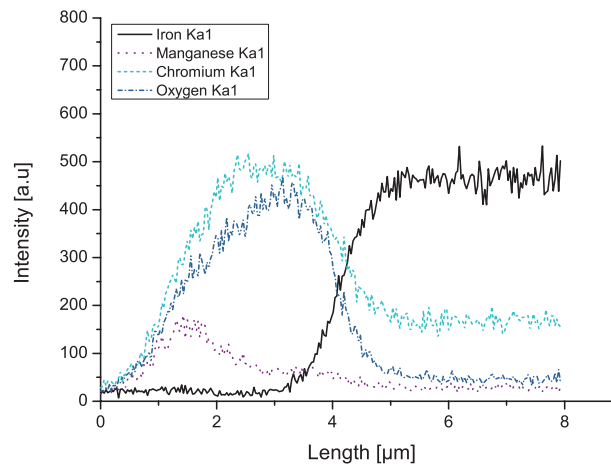


Figure 4.13: EDX line scan of a lanthanum-coated sample cross-section exposed for 500 h.

observed in the uncoated material, two FIB cross-sections, one of an uncoated sample and one of a cerium-coated sample, were prepared. This was done to exclude potential contamination caused by the polishing process. Figure 4.14 shows an EDX line scan of the uncoated sample and Figure 4.15 shows the same for the cerium-coated sample. It is clear that in both cases a subscale silica layer has been formed. This confirms the conclusion of Jablonski et al. that sub-scale silica formation is caused by insufficient silicon capture in the Laves phases [15]. In this context, it is not clear whether subscale silica formation alone causes oxide scale spallation. Both reactive element coatings improved scale adhesion. Even though the exposure temperatures for observing a reactive element effect are relatively low, these observations are in line with those made in other studies [68,69]. Several researchers have proposed mechanisms for this beneficial effect, including a reduction in growth rate, change in from inward to outward growth, or vice versa, a higher scale plasticity, reduction in growth stress, and improved scale-alloy interface [70,71]. Based on these investigations, it is concluded that the observed spallation is not exclusively due to sub-scale silica formation. A beneficial effect of the cerium coating in preventing silica subscale formation, as reported by Alman et al. could not be confirmed [26]. One might suspect a combination of weakened scale adhesion (due to silica formation) and the presence of growth stresses as being the cause of the scale spallation. Growth stresses can be decreased by reactive element coatings, thereby preventing scale spallation.

In comparison to the uncoated and the reactive element-coated materials, the surfaces of the cerium/cobalt-coated samples (example shown in Figure 4.16) appeared to be much smoother. This smoothing effect was also seen in the cross-sectional micrograph (Figure 4.17). The observed double-layer oxide appeared, due to the cobalt top coating, to be much thicker (about $1.9 \mu\text{m}$) in the outer oxide layer and relatively thin ($1.4 \mu\text{m}$) in the inner oxide layer. The outer oxide layer was rich in cobalt and manganese, whereas the inner oxide layer was mostly composed of chromium oxide,

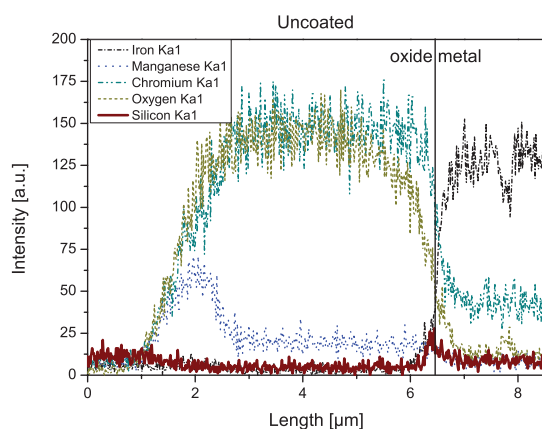


Figure 4.14: EDX line scan of a FIB-prepared uncoated sample exposed for 500 h.

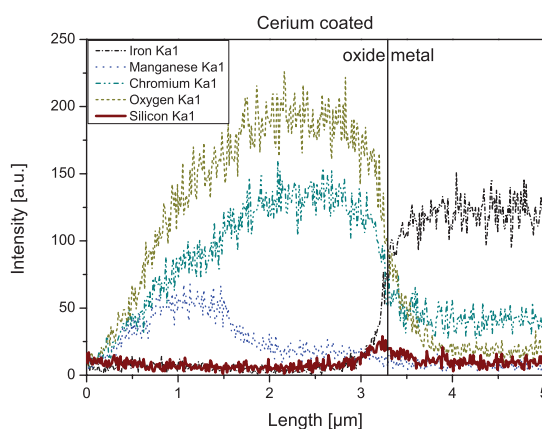


Figure 4.15: EDX line scan of a FIB prepared cerium-coated sample exposed for 500 h.

as the EDX line scan shows (Figure 4.18). As in the previous cases, internal oxidation and Laves phases were observed. The observed smoother surface is assumed to be a result of the cobalt top coating, which was deposited as metal. The large volume expansion during initial oxidation led to an evening-out of the linear texture. That this texture was only present on the uncoated and reactive element-coated sample surfaces might be explained by the rolling marks present in the steel (and introduced during production) prior to exposure. The surface of a lanthanum/cobalt-coated sample is shown in Figure 4.19. It is evident that the surface is slightly wavier in texture than the cerium/cobalt-coated material. The cross-section (Figure 4.20) confirms this increase in waviness. An EDX line scan (Figure 4.21) did not show any major compositional differences between the lanthanum/cobalt-coated sample and the cerium/cobalt-coated samples. The increased waviness might be due to the extensive bendiness of the material observed after removal from the furnace. This was subsequently confirmed by observations of the backside of the sample, which had a much less wavy texture.

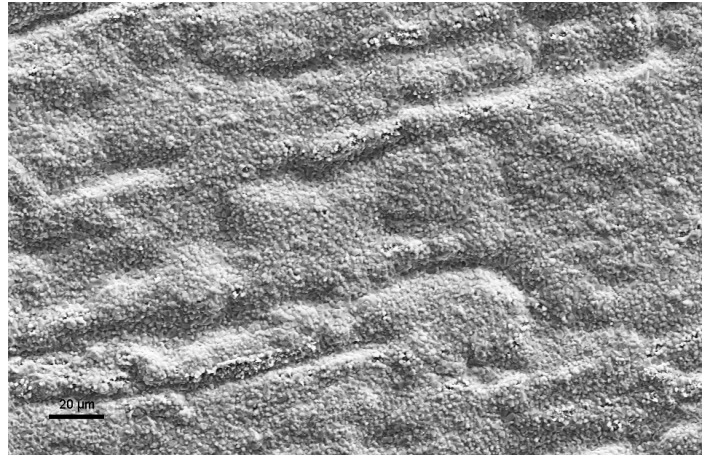


Figure 4.16: Topview of a cerium/cobalt-coated sample exposed for 500 h.

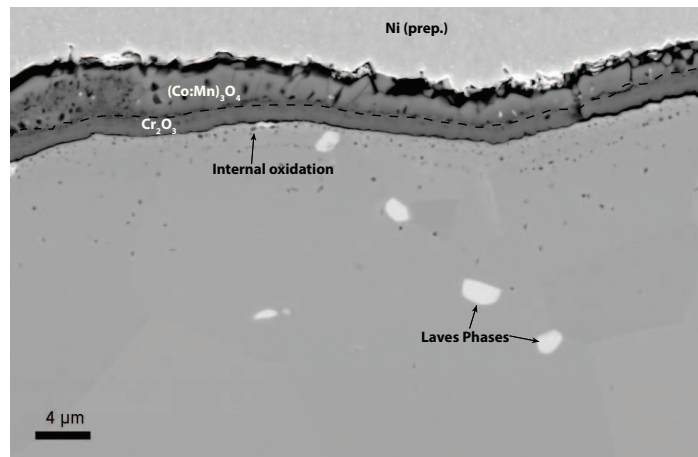


Figure 4.17: Cross-section of a cerium/cobalt-coated sample exposed for 500 h.

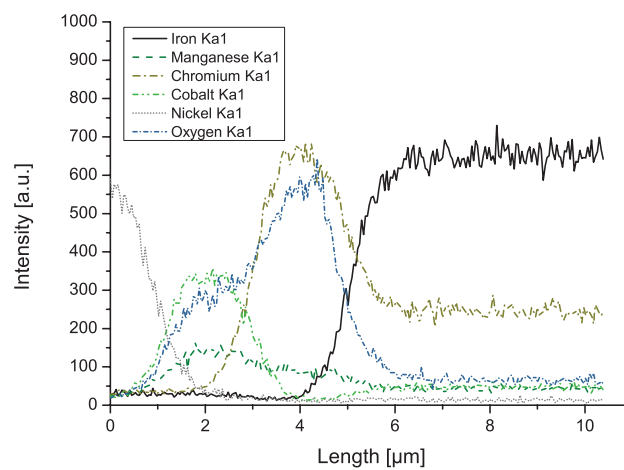


Figure 4.18: EDX line scan of a cerium/cobalt-coated sample cross-section exposed for 500 h.

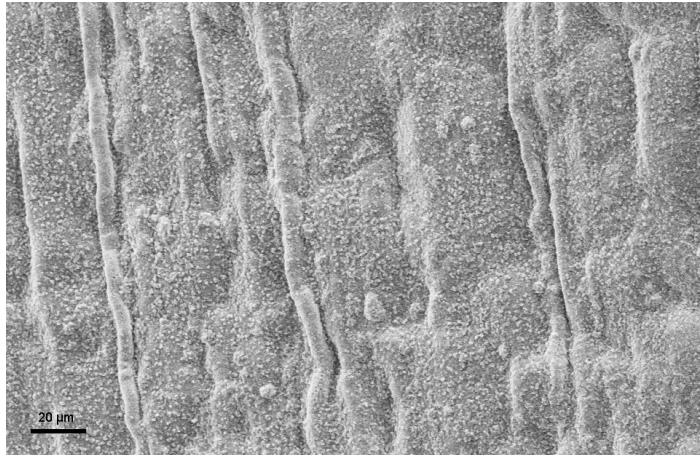


Figure 4.19: Topview of a lanthanum/cobalt-coated sample exposed for 500 h.

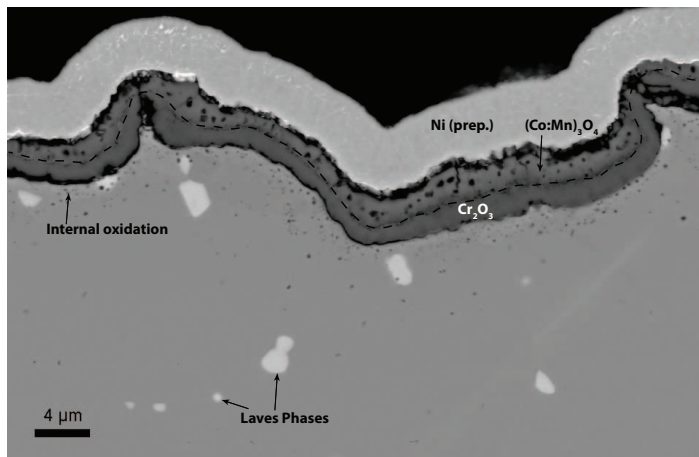


Figure 4.20: Cross-section of a lanthanum/cobalt-coated sample exposed for 500 h.

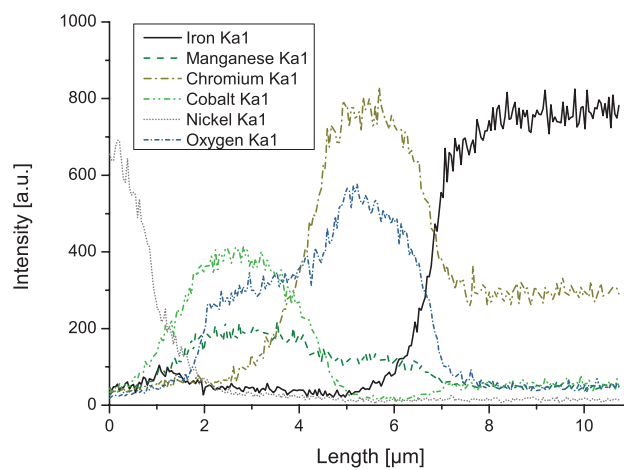


Figure 4.21: EDX line scan of a lanthanum/cobalt-coated sample cross-section exposed for 500 h.

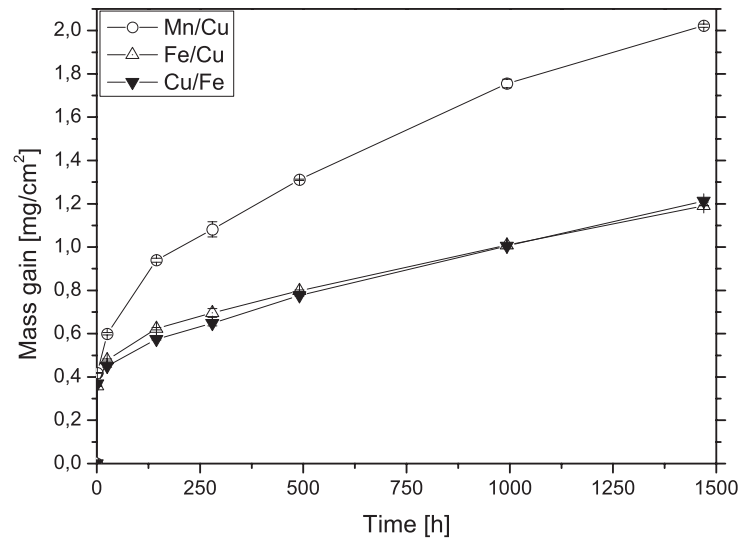


Figure 4.22: Mass gain of stainless steel Sandvik Sanergy HT with different copper conversion coatings.

4.1.3 Sanergy HT with copper based conversion coatings

The second investigation was designed to examine the properties of the Sandvik Sanergy HT coated with copper/manganese and copper/iron spinel-forming coatings in a cathode atmosphere. These coatings were chosen because of the lower material price of copper, as compared to cobalt, and the high theoretical electrical conductivities of copper spinels.

4.1.4 Mass gain

The mass gain was measured during discontinuous exposures at intervals of increasing duration. The mass gain for 1500 h of exposure time is plotted in Figure 4.22. Both copper/iron coatings performed similarly, achieving a mass gain of 1.2 mg/cm² after being exposed for almost 1500 h. The manganese/copper-coated material gained substantially more mass, reaching a value of 2.0 mg/cm² for the same exposure time. Compared to the result obtained previously at the research group of the HTC for cobalt-coated Sandvik Sanergy HT, i.e., a mass gain of approximately 1.5 mg/cm² after 1500 h exposure time, the copper/iron coatings showed significantly lower mass gain, while the mass gain for the manganese/copper coating was much higher the previous values [64].

4.1.5 Chromium evaporation

The levels of chromium evaporation for the manganese/copper-coated, copper/iron-coated, and iron/copper-coated materials were measured for 500 h, while the copper/iron-coated material was assessed for 1000 h. The chromium evaporation is shown

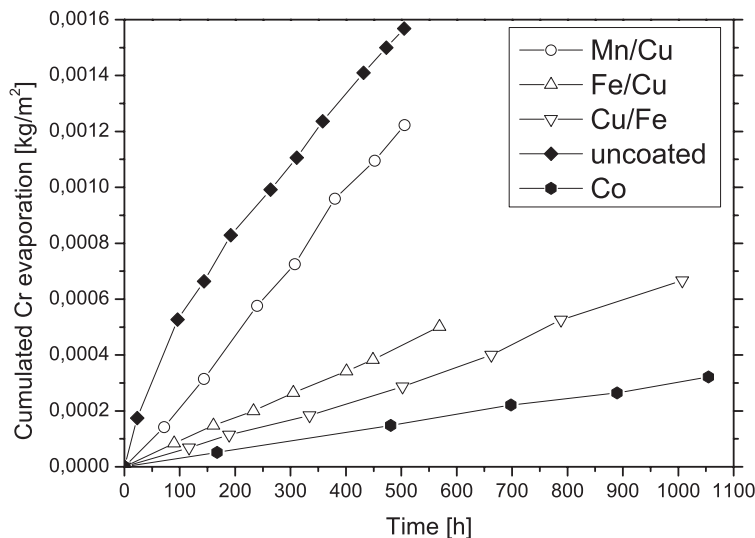


Figure 4.23: Chromium evaporation of stainless steel Sandvik Sanergy HT with different copper conversion coatings, compared to uncoated and cobalt-coated [64].

in Figure 4.23. The manganese/copper-coated material evaporated a total mass of 0.0012 kg/m^2 after an exposure time of 500 h, and the iron/copper-coated material evaporated approximately 0.0005 kg/m^2 after 500 h of exposure. The copper/iron-coated material released a mass of 0.00028 kg/m^2 after 500 h and after the total exposure time of 1000 h, a cumulated evaporation of 0.00067 kg/m^2 was noted. Compared to the uncoated Sandvik Sanergy HT, the manganese/copper coating had almost no effect on chromium evaporation, while the iron/copper and copper/iron coatings decreased chromium evaporation by 50 % to 70 % and about 80 %, respectively. Compared to the cobalt-containing coatings, which decreased chromium evaporation by about 90 %, the copper/iron coating was almost as effective at chromium retention [64].

4.1.6 Microstructural evolution

After exposing the samples to a cathode-side atmosphere continuously for 500 h, a microstructural investigation was carried out. The cross-sectional micrograph of a manganese/copper-coated sample and a corresponding EDX line scan are shown in Figures 4.24 and 4.25, respectively. The total oxide thickness of the double-layered oxide was about $10 \mu\text{m}$. The oxide scale was detached at several locations, and pores were observed at the metal/oxide interface. The outer oxide layer consisted mainly of copper and manganese, with relatively high levels of chromium, whereas the inner oxide layer contained mainly chromium oxide.

The manganese/copper-coated samples did not show improved properties in terms of chromium evaporation and corrosion. The coating was not considered to be beneficial for interconnect performance at $850 \text{ }^\circ\text{C}$. This observation is in line with the findings of Wei et al. who have investigated similar coatings of manganese and copper on

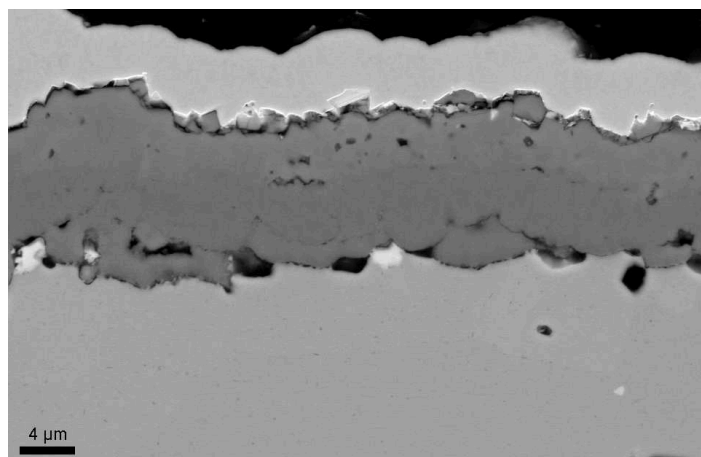


Figure 4.24: Cross-sectional SEM micrograph of a manganese/copper-coated sample exposed for 500 h.

UNS 430 at different temperatures [72]. They observed, as it was the case in the present work, pores within the oxide scale and deduced a maximum operational temperature of about 750 °C. At temperatures of 850 °C and above, the substrate used in their study suffered from severe corrosion, while at temperatures below 850 °C almost no chromia was formed beneath the coating. This may explain our observation (in the present work) of relatively high levels of chromium evaporation due to breakdown of the protective scale. In an earlier study, Paulson and colleagues mentioned the diffusion of iron and chromium through copper manganese coatings [73]. In the present work, a different ratio of copper to manganese was employed than that used by Paulson et al., and this could be a reason for the relatively high level of corrosion observed [73]. The manganese/copper coating might be more effective in mitigating chromium volatilization at lower operational temperatures, although at the investigated temperature it was not effective.

The cross-section of a iron/copper-coated sample, shown in Figure 4.26, revealed a stronger contrast in the double-layer oxide. With a total oxide thickness of about 5 μm , the oxide was about 50 % thinner than that in the manganese/copper-coated samples. Furthermore, a well-adhered oxide scale was present over the entire sample surface, and almost no pores were observed at the metal/oxide interface. The EDX line scan analysis (Figure 4.27) showed an outer oxide layer that consisted mainly of copper and iron with chromium and some manganese, whereas the inner oxide layer mainly contained chromium oxide with a small fraction of manganese. With respect to chromium evaporation and oxidation rate, the coating that comprised an inner copper layer with an outer iron layer performed best among the copper conversion coatings tested. Therefore, it was decided to investigate the microstructural evolution of this material in more detail. In Figure 4.28, a cross-section of a copper/iron-coated sample after 100 h is shown, and a layered oxide structure is also evident in the cor-

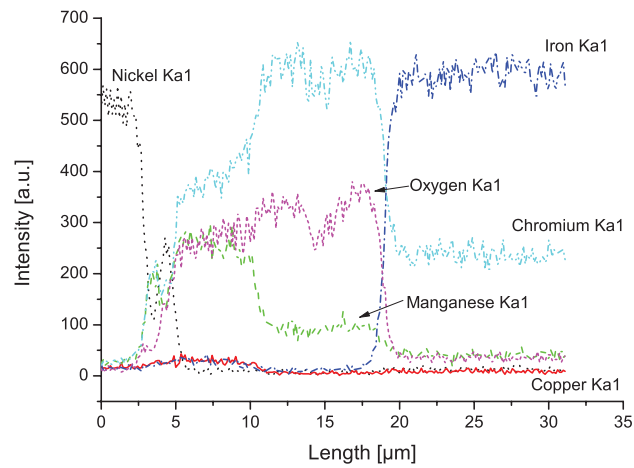


Figure 4.25: EDX line scan of a manganese/copper-coated sample exposed for 500 h.

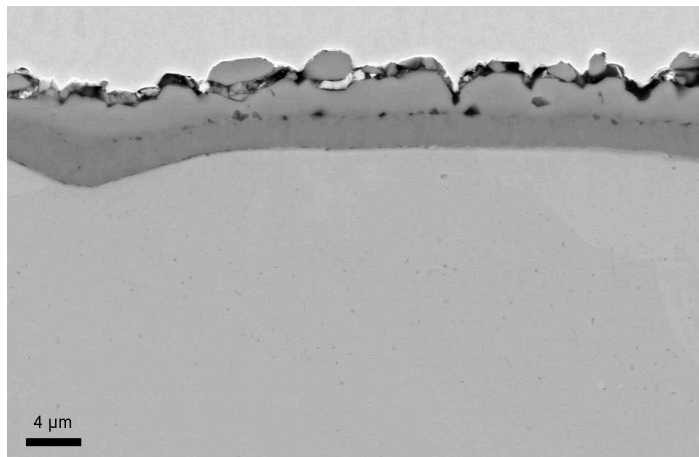


Figure 4.26: Cross-sectional SEM micrograph of a iron/copper coated sample exposed for 500 h.

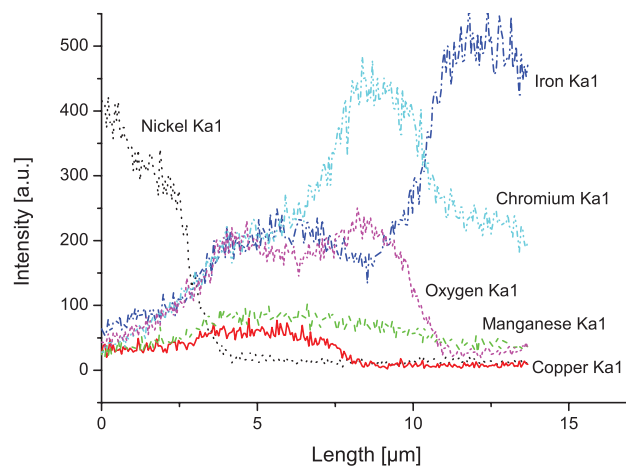


Figure 4.27: EDX line scan of a iron/copper coated sample exposed for 500 h.

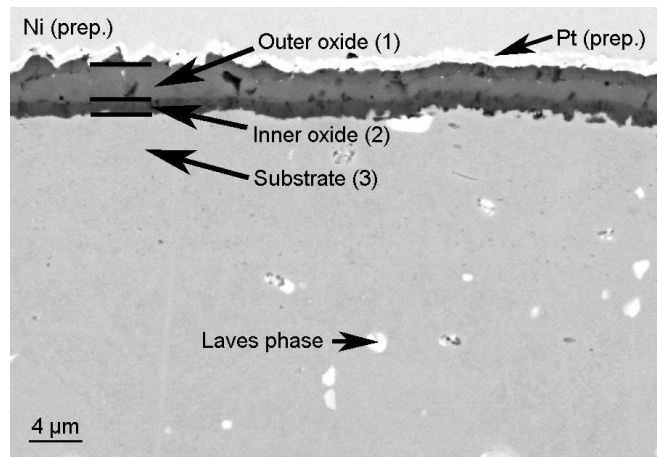


Figure 4.28: Cross-sectional SEM micrograph of a copper/iron-coated sample exposed for 100 h.

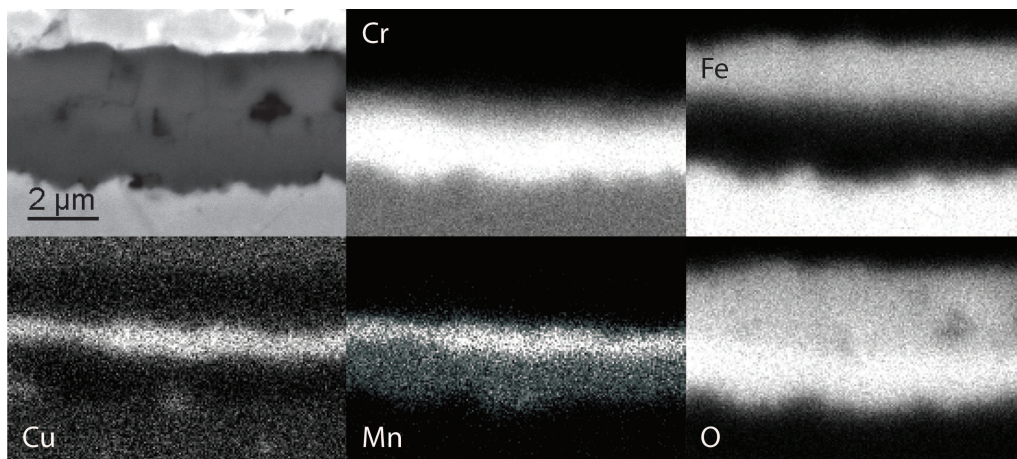


Figure 4.29: EDX-map of a copper/iron-coated sample exposed for 100 h.

responding EDX map (Figure 4.29). The inner oxide is chromium-rich, whereas the outer oxide appears to be composed of several layers that are rich in copper, iron and manganese. After 1000 h of exposure, the oxide structure appears more ordered, as evidenced by the cross-section (Figure 4.30) and corresponding EDX map (Figure 4.31). An XRD scan of a sample after 1000 h is shown in Figure 4.32, both a spinel phase and an eskolite phase were detected. Based on the analyses of the microstructure and crystal structures, it can be concluded that the copper/iron coating forms a well-adhered oxide scale with a spinel crystal structure. It appears that after only 100 h of exposure the oxide structure is not yet as ordered as it is after 1000 h of exposure, since in the first case (after 100 h of exposure) the copper-rich layer seems to be separated from the iron-rich layer. This might be due to relatively slow intermixing of the copper and iron oxide layers. After 1000 h, in contrast, the outer oxide appears to be relatively uniform. An important aspect of the copper/iron coating

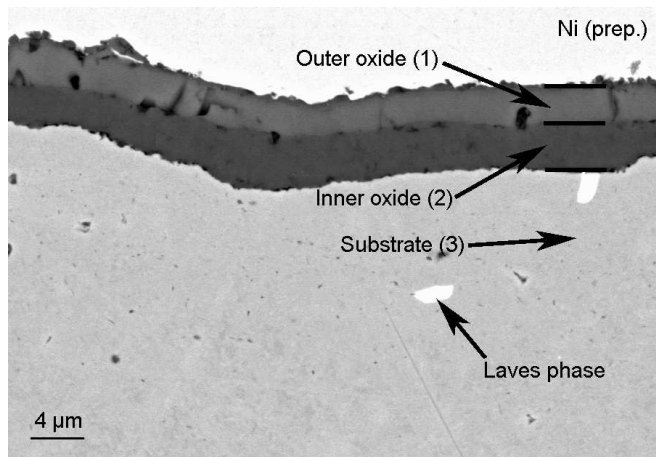


Figure 4.30: Cross-sectional SEM micrograph of a copper/iron-coated sample exposed for 1000 h.

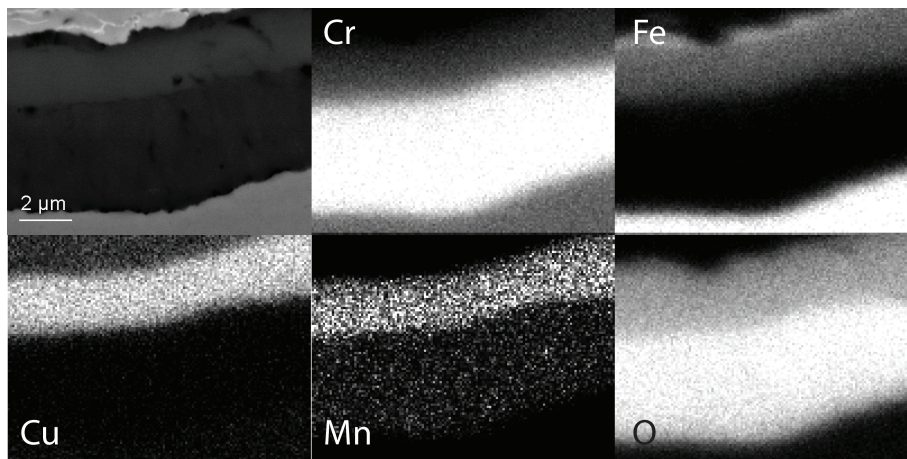


Figure 4.31: EDX-map of a copper/iron-coated sample exposed for 1000 h.

is the observed outward diffusion of manganese. This has been observed previously for cobalt conversion coatings [42]. In the case of a copper/iron spinel, the outward diffusion of manganese might lead to a larger lattice parameter and a decrease in electrical conductivity, as described by Salah et al. [74]. Whether this effect significantly changes the material properties, giving longer exposures and different coating thicknesses, needs to be investigated further. In general, the copper/iron coating appears to be promising, and might even have better performance when exposed at lower temperatures, due to a lower rate of outward diffusion of manganese.

4.1.7 Alternative coatings for chromium retention

Coatings of zinc for chromium retention were prepared by electro-plating and tested for chromium evaporation, as alternative to the coatings prepared by Sandvik Materi-

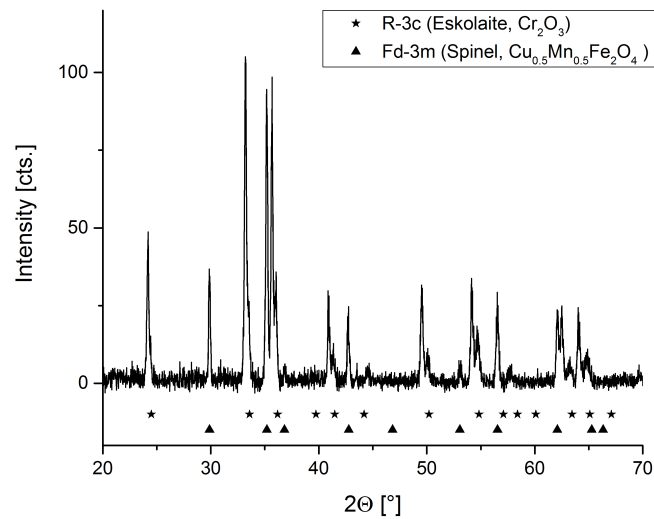


Figure 4.32: XRD pattern of copper iron coated Sanergy HT after 1000 h of exposure.

als Technology. The aim was to investigate an electroplated coating of zinc, which was thought to form zinc oxide and was supposed to be doped with aluminum eventually. In contrast to the other chromium evaporation measurements, these exposures were started in a cold furnace, which was then slowly heated to 850 °C, in order to avoid melting of the zinc coating during the early stages of exposure. The evaporation of chromium from the zinc-plated Sanergy HT steel is plotted in Figure 4.33. It can be seen that the level of evaporation of chromium was about three-fold lower than that of cobalt/cerium-coated AISI 441. The lower level of chromium evaporation may be due to the fact that the thickness of the zinc coating was probably in the range of a few micrometers. Since, in previous studies at HTC, ceramic coatings with thicknesses of several micrometers performed only equally as well as cobalt coatings, a chromium retention effect of the zinc coating seems reasonable [41]. It was not clear if the zinc coating itself suffered from evaporation. Further investigations of the microstructural evolution and the potential evaporation of zinc are planned.

4.2 Electrical properties

The second part of this thesis focuses on the electrical properties of selected substrate coating combinations that have been shown in previous experiments to have good corrosion performances and low levels of chromium evaporation. Moreover, the electrical properties of different model oxides are investigated.

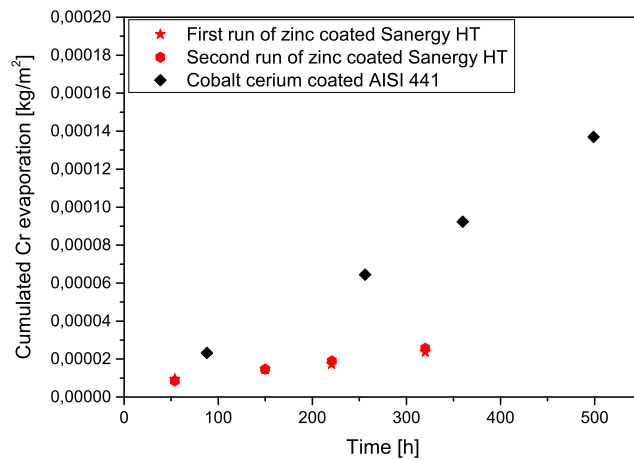


Figure 4.33: Chromium evaporation of zinc coated Sanergy HT, AISI 441 coated with cobalt cerium for comparison.

4.2.1 Electrical properties of chromia

All the investigated substrates are chromia-forming alloys. The conductivity of chromia significantly influences the conductivity of an oxide scale growing on an interconnect. There are many values available in the literature for the conductivity of chromia, as described in Section 2.3.3. To relate these values to the investigated sample systems it was decided to investigate the conductivity of chromia that was synthesized by different methods. Hot-pressed chromia, chromia grown on pure chromium, and chromia grown on a model alloy of iron with 20 % chromium at two different temperatures (850 °C and 950 °C) were prepared, and their electrical conductivities were measured at different temperatures. The measured conductivity values are shown in Figure 4.34. There were significant differences between the measurements for the chromia pellet and the chromia grown on metallic samples. This might be due different levels of impurities and the fact that heat treatments improved the conductivity of the chromia pellets at high temperatures and changed the activation energy at low temperatures. The activation energies for electronic conduction for the pellets were: 0.5 eV in the "as received" state; 0.65 eV after quenching from 1400 °C; and 0.59 eV after the sample had been thermally relaxed by a slow cooling down procedure from 1400 °C. Chromia grown on pure chromium had an activation energy of 0.47 eV below a temperature of 600 °C, where the curve was linear. Both chromia systems grown on the iron 20 wt.% chromium model alloy showed linear behaviors over the investigated temperature range, and they had activation energies of 0.45 eV for the samples exposed at 950 °C and 0.52 for the samples exposed at 850 °C. It should be borne in mind that the oxide scales on the metallic samples were only approximately 1 μm thick and that the electrodes used were porous, as shown in Figure 4.36. As a consequence, not all of the oxide contributes to conduction and since the derived

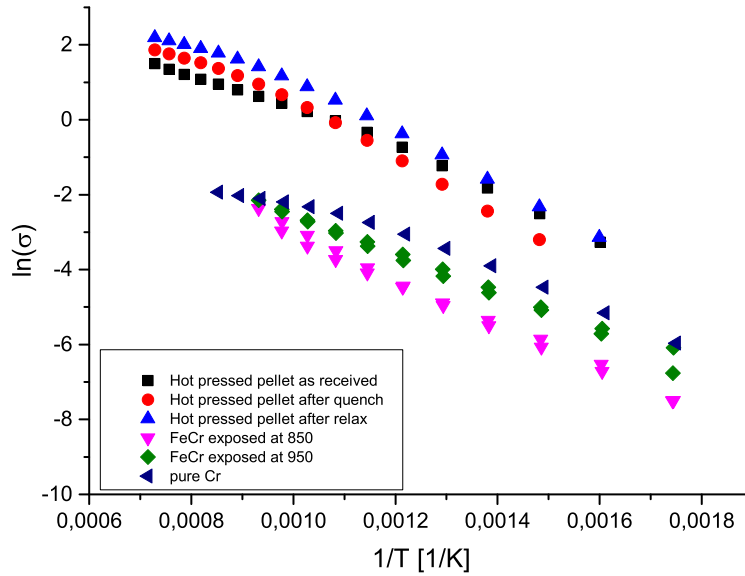


Figure 4.34: Electrical conductivity of investigated chromia systems.

conductivity values are based on the incorrect volume, they are too low. A simplified model that allows one to compensate for this effect has been described previously [75]. It was assumed that in the case of the iron 20 wt.% chromium model alloy only about 20 % of the volume contributed to conduction. The compensated conductivity of the samples exposed at 950 °C and also the "as received" conductivity of the chromia pellet were compared to the values provided in the literature (Figure 4.35). It is clear that with this compensation, the conductivity values for the iron 20 wt.% chromium model alloy are well within the literature values and that the conductivity of the chromia pellet lies within the upper limit of the literature values. Since only some of the used references provided activation energies for the electronic conduction and not always with the relevant temperature interval, all the available literature data derived at temperatures below 850 °C were fitted, and the activation energy was calculated using the Arrhenius equation. The calculated values are summarized in Table 4.1. It can be seen that most of the values are in the range of 0.4 to 0.5 eV, which is in good accordance with the findings for the chromia oxide scales grown on the metallic samples, as well as most of the activation energies derived for the samples tested in the work for this thesis.

4.2.2 AISI 441 coated with cobalt cerium

The first interconnect coating substrate system investigated in this thesis involved AISI 441 coated with different nano-coatings. During this investigation, the coating with cerium and cobalt proved to be most effective in improving the corrosion

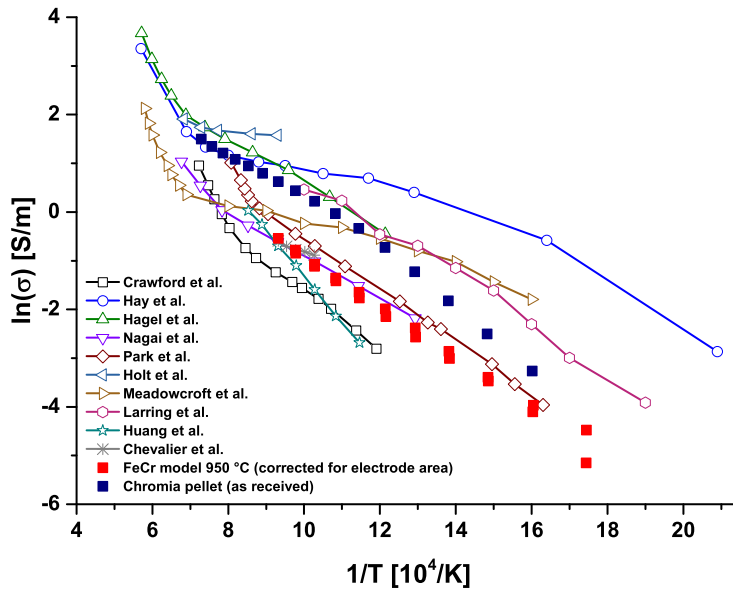


Figure 4.35: Electrical conductivity of chromia samples compared to literature values.

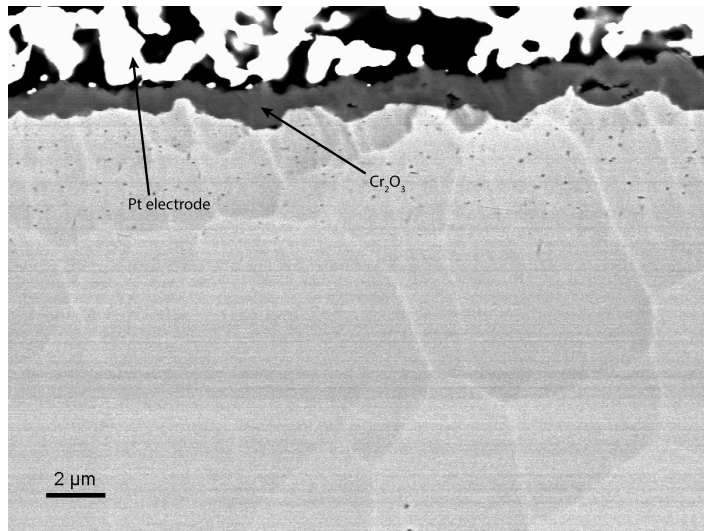


Figure 4.36: Cross section of a iron 20 wt.% chromium model alloy exposed at 950 °C after electrical characterization.

Publication	Year	Activation energy	Std. error on fit
Hagel and Seybold	1961	0.44 eV	4.5 %
Crawford and Vest	1964	0.51 eV	3.8 %
Hay et al.	1970	0.27 eV	11.2 %
Meadowcroft and Hicks	1972	0.22 eV	7.1 %
Nagai et al.	1983	0.37 eV	1.2 %
Park and Natesan	1990	0.46 eV	0.9 %
Huang et al.	2001	0.82 eV	1 %
Larring et al.	2003	0.43 eV	4 %
Chevalier et al.	2009	0.25 eV	11.1 %

Table 4.1: Activation energy for electronic conduction in chromia derived from literature values at temperatures below 850 °C taken from [46, 48, 50–52, 54–57].

properties and lowering the evaporation of chromium. Therefore, it was selected for characterization of its electrical properties. The samples were measured using the Solartron 1260A Impedance Analyzer at a frequency of 1 Hz, since a DC system was not yet available for the characterization. This study was also aimed at investigating the long-term effects of the platinum electrodes on the microstructures of the samples, as is commonly described in the literature [39, 40, 76]. Therefore, two types of measurements were performed: 1) *ex situ* samples with long pre-oxidation times were measured for only short periods of time (less than one hour); and 2) *in situ* samples were measured for up to 500 h at 850 °C. The *in situ* samples were pre-oxidized for only 60 min, to avoid direct contact between the platinum electrodes and the metal, and were cooled down at regular intervals, to allow activation energy calculations. The evolution patterns of the ASR values of the individual *ex situ* samples and one *in situ* sample are shown in Figure 4.37. Due to failure of the measurement software, the electrical measurement was interrupted for 75 h after about 130 h of exposure, and the setup was not cooled down during that time period. It can be seen that the *in situ* measured sample showed dramatic increases in the ASR values after only very short exposure times. After the total exposure time of 500 h, an ASR value of 35 mΩcm² was reached for the *in situ* sample. The *ex situ* measured samples showed a large variability after 60 min of exposure, whereas only moderate increases in ASR values were noted after longer pre-oxidation times, with an ASR value of 15 mΩcm² being reached after more than 1500 h of exposure. Furthermore, the activation energy of the electrical conduction was calculated by measuring the ASR at different temperatures (during the cooling down period). The activation energies for the different *ex situ* samples and the *in situ* sample are plotted in Figure 4.38.

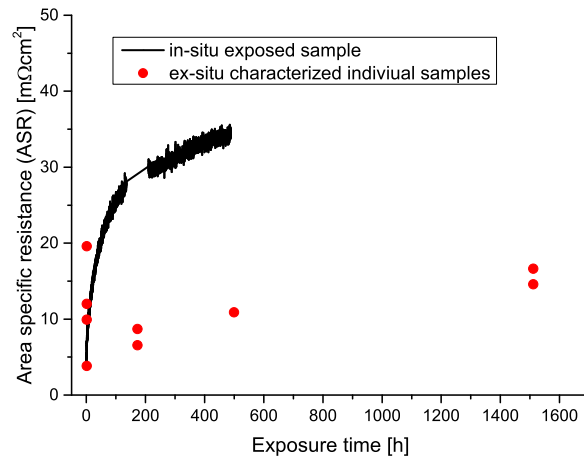


Figure 4.37: Area specific resistance of cerium cobalt coated AISI 441 exposed at 850 °C in air.

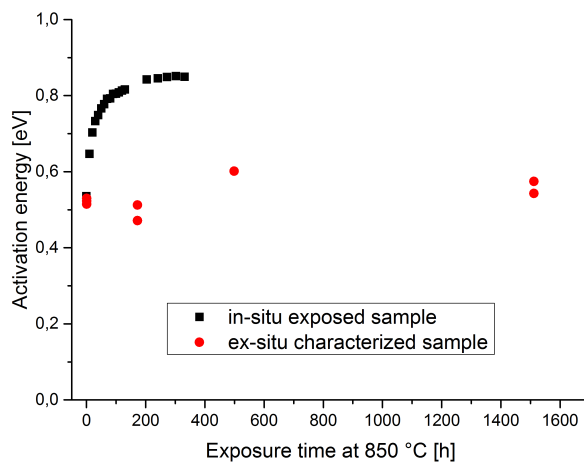


Figure 4.38: Evolution of the activation energy for the electrical conduction of cerium cobalt coated AISI 441 exposed at 850 °C in air.

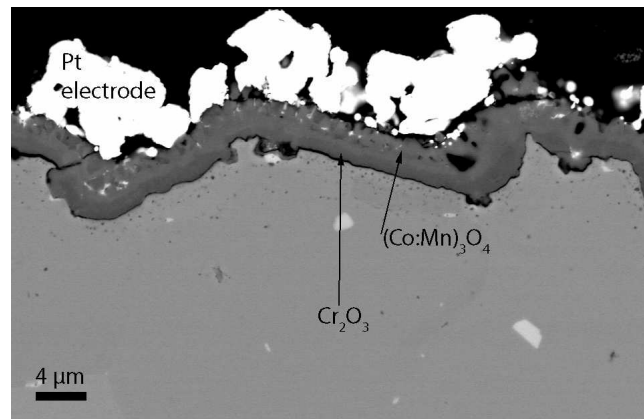


Figure 4.39: Cross-sectional SEM micrograph of a cerium cobalt coated 441 sample exposed for 500 h after ex-situ ASR characterization.

It can be seen that the activation energy remains relatively constant for the *ex situ* measured samples, with values between 0.49 eV and 0.61 eV, whereas the *in situ* measured sample shows a rapid increase in activation energy from an initial value of 0.55 eV to 0.85 eV. This rapid increase in activation energy for the *in situ* measured sample suggests that the characterization influences the oxide scale growth; two SEM cross-sections were prepared to investigate further this phenomenon. Figures 4.39/4.40 and 4.41/4.42 depict a cross-section and an EDX line-scan of an *ex situ* measured samples, exposed for 500 h and a cross-section and an EDX line-scan of the *in situ* measured sample after 500 h of measurement, respectively. It is clear that the *in situ* measured sample has a significantly different microstructure and much thicker oxide scale. Furthermore, the iron and chromium contents are dramatically higher for the *in situ* tested sample. While one might suspect that the observed effect could be due to the applied current, in the context of the observations made by Kawamura et al. and Kodjamanova et al., this seems unlikely in this case since the period of measurement was only 0.1 % of the overall measurement time [77, 78]. Alternatively, the observation might be attributable to thermal cycling, although this also seems unlikely, since similar samples that were not cycled did not show the same effect. Instead, it is probable that the change in oxide scale is due to an effect of platinum on the oxidation, similar to the phenomenon reported by Dong et al. [79]. Thus, it can be concluded that during the investigated time-frame of 1500 h of exposure, AISI 441 shows promising electrical properties, and that long-term measurement, using platinum electrodes seems not to be appropriate.

4.2.3 Effect of cerium in a cobalt coating

Previous works conducted at the research group of the HTC investigated extensively the protective properties of coatings of cobalt and cobalt in combination with cerium on Sanergy HT at 850 °C in air [41, 42, 64, 65]. As a result, it was decided to investigate the effect of cerium on the conductivities of the spinel layers in these types of

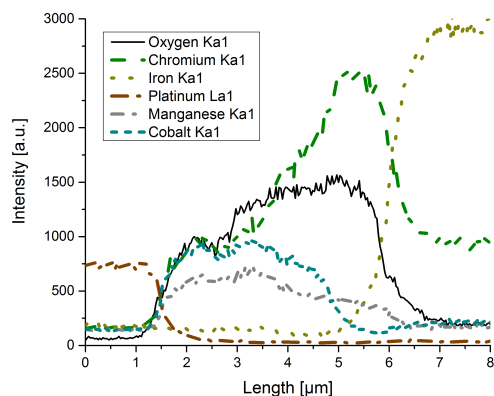


Figure 4.40: EDX line scan of a cerium cobalt coated 441 sample exposed for 500 h after ex-situ ASR characterization.

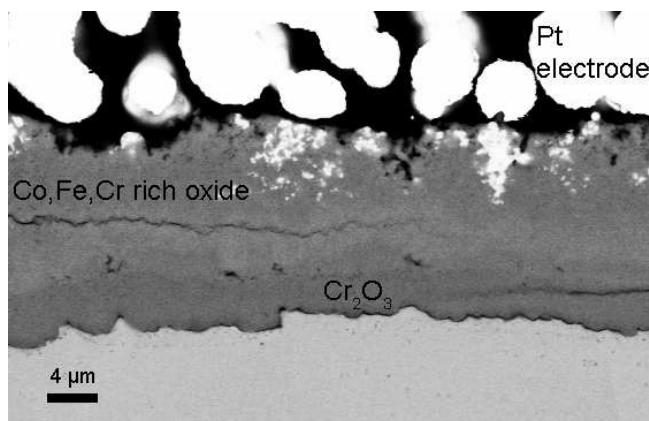


Figure 4.41: Cross-sectional SEM micrograph of a cerium cobalt coated 441 sample exposed for 500 h after in-situ ASR characterization.

coatings. Two strategies were used to address this issue: 1) samples were exposed for different times; and 2) DC-characterized (from 2 h up to 3300 h) and selected samples were subjected to additional measurements using impedance spectroscopy at low temperatures. The evolution patterns of the ASR values of the two investigated sample systems are shown in Figure 4.43. The ASR values of both sample systems increased with increasing exposure time. After a total exposure time of 3300 h, ASR values of $39 \text{ m}\Omega\text{cm}^2$ and $21 \text{ m}\Omega\text{cm}^2$ for the cobalt-coated and the cobalt/cerium-coated samples, respectively, were reached. At all the investigated time intervals, the cobalt-coated samples had higher ASR values than the cerium/cobalt-coated samples. Both sample systems showed a relatively linear relation between mass gain and ASR, see Figure 4.44. Interestingly, there were no significant differences between the cobalt-coated and cobalt/cerium-coated samples in this plot. Similar observations were made concerning the activation energy. For both sample systems, a decrease in

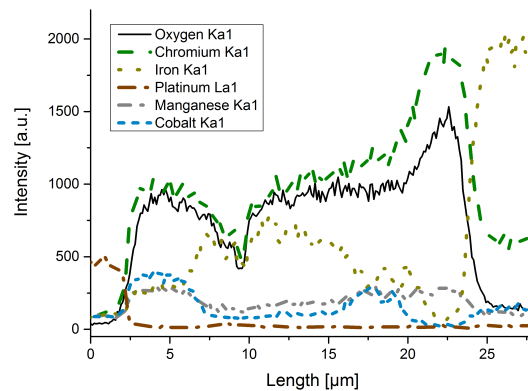


Figure 4.42: EDX line scan of a cerium cobalt coated 441 sample exposed for 500 h after in-situ ASR characterization.

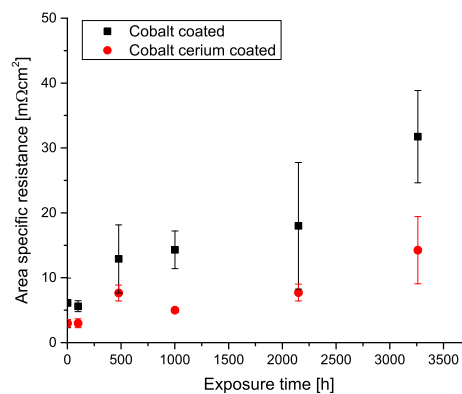


Figure 4.43: Area specific resistance of cobalt and cerium cobalt coated Sanergy HT exposed at 850 °C in air.

activation energy from about 0.6 eV to 0.45 eV was observed, which is plotted over the mass gain in Figure 4.45.

Besides the DC characterization impedance spectroscopy was used to reveal the contribution from the individual oxide layers to the ASR. An example of a Nyquist plot of a cobalt and a cobalt cerium coated sample after more than 3000 h of exposure at 850 °C taken at a temperature of 150 °C can be seen in Figure 4.46. Since the investigated oxide scales were comparably conductive, impedance spectroscopy proved to be challenging. This was due to the fact that at high temperatures, the resistances of the samples were too low, so the observed signal-to-noise ratio was too high. At a temperature interval from 200 to 50 °C the signal-to-noise ratio obtained was low enough to allow reasonable evaluation. The obtained Nyquist plots were fitted with an equivalent circuit of two in-series-connected R/CPE elements (Figure 4.47). The

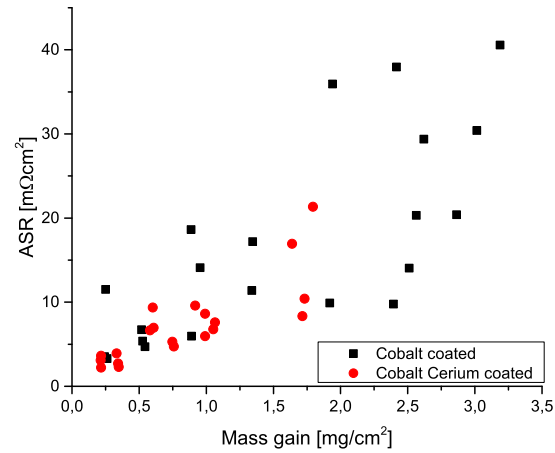


Figure 4.44: Area specific resistance versus mass gain of cobalt and cerium cobalt coated Sanergy HT exposed at 850°C in air.

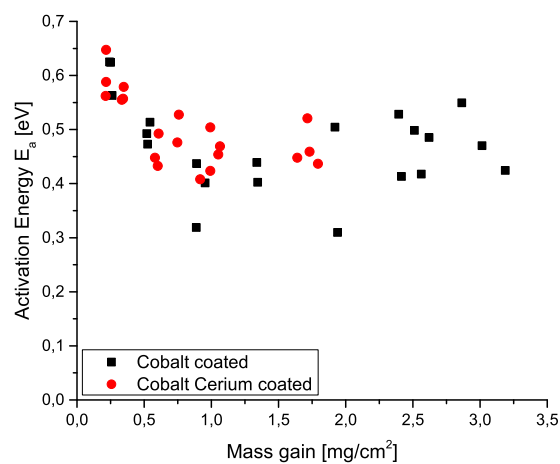


Figure 4.45: Activation energy evolution over mass gain of cobalt and cerium cobalt coated Sanergy HT exposed at 850°C in air.

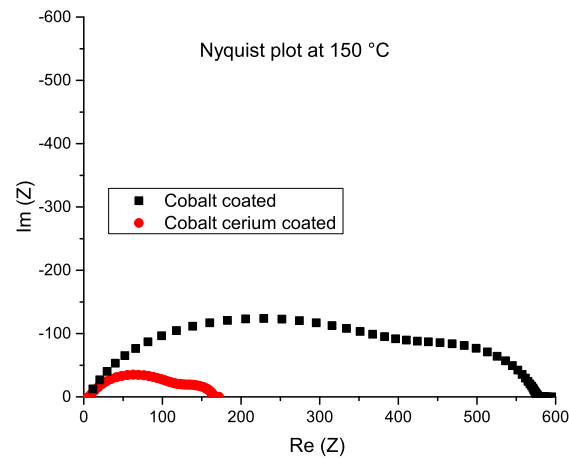


Figure 4.46: Nyquist plot of a cobalt and a cerium cobalt coated Sanergy HT sample exposed at 850 °C in air for 3300 h taken at 150 °C.

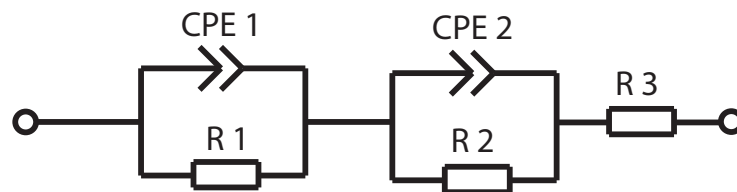


Figure 4.47: Equivalent circuit used for fitting of Nyquist plots.

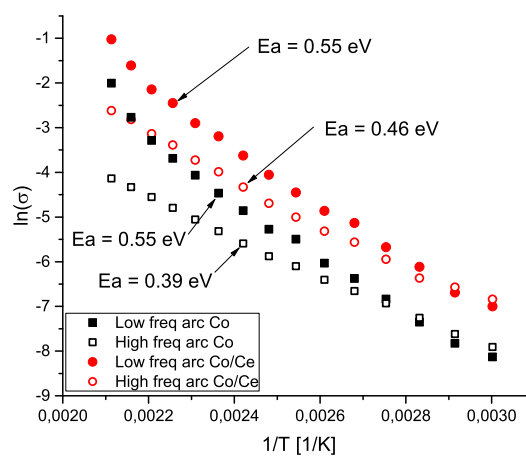


Figure 4.48: Arrhenius plot of from IS measurement of a cobalt and a cerium cobalt coated Sanergy HT sample exposed at 850 °C in air for 3300 h.

conductivity values derived from fitting the Nyquist plots for two samples exposed for longer than 3000 h obtained in the interval from 200 to 50 °C are plotted in Arrhenius fashion in Figure 4.48. It can be seen that for the cobalt-coated sample, the conductivities of the two R/CPE elements are lower than that for the cobalt/cerium-coated sample. The activation energies for the conductivity values derived from the low frequency arc were 0.55 eV for both samples, whereas the activation energies for the conductivity derived from the high frequency arc were 0.39 eV and 0.45 eV for the cobalt-coated and the cobalt/cerium-coated samples, respectively. To assign the individual semi-circles observed in the Nyquist plots to the individual oxide layers, two strategies were used. The activation energies for the values derived from the low frequency circle were similar to the activation energies after very short exposure times. Since the oxide scale that is present after very short exposure times mainly consists of cobalt manganese spinel, one can assume that the activation energy for the electrical conduction of these samples is similar or equal to the activation energy of a cobalt manganese spinel. The values given in the literature for the activation energies of cobalt manganese spinels are in the range of 0.55 to 0.76 eV, which indicates that the low frequency arc represents the cobalt manganese spinel [43, 75, 80, 81]. Besides the activation energy, one could also consider that the peak frequency of an R/CPE element is the inverse of the product of capacitance and resistance, and since the capacitance of the cobalt manganese spinel is expected to be high compared to that of the chromia scale (owing to the oxide scale of the former being less thick), this is further indication that the low frequency arc is caused by the cobalt manganese spinel.

After short exposure times (less than 100 h), the ASR can be considered to be dominated by the electrical properties of the spinel layer. The cobalt-coated samples had already after short exposure times significantly higher ASR, which means that there were differences in the electrical properties of the spinel layer between the cobalt-coated and the cobalt/cerium-coated samples (the cobalt-coated samples being less conductive). In addition, during the impedance measurements, it was observed that the conductivity derived from the low frequency arc, which was identified as the cobalt manganese spinel layer, was lower in the case of the cobalt-coated sample. This observation was consistent over the entire time-frame (1000 to 3300 h) investigated using impedance spectroscopy. Thus, it can be concluded that the spinel layer in the cobalt-coated case is less conductive than that in the cobalt/cerium-coated case. A possible explanation for this observation is the higher content of iron in the cobalt-coated samples, as reported previously by Canovic et al. [42]. Iron is considered to lower the conductivity of cobalt manganese spinels when added in sufficient amounts [81, 82].

4.2.4 Copper iron spinel coating on Sanergy HT

Amongst the group of copper conversion coatings, the coatings that contained copper and iron showed the best performances in terms of chromium evaporation and corro-

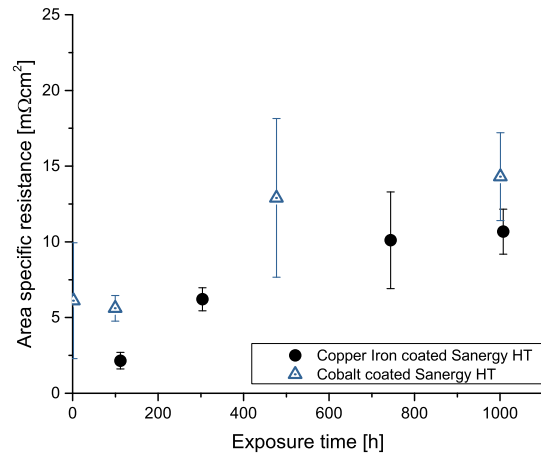


Figure 4.49: Area specific resistance of copper iron coated Sanergy HT exposed at 850 °C in air, cobalt coated Sanergy HT for comparison.

sion protection (see Section 4.1.3). Therefore, the electrical properties of these types of coating were investigated. The evolution of the ASR values is plotted in Figure 4.49. It can be seen that after about 1000 h of exposure at 850 °C an ASR value of 10 mΩcm² was reached. Furthermore, the evolution of the ASR values followed a trend similar to that of the mass gain, if one neglects the initial mass gain (see Figure 4.22). The activation energies derived from the cooling-down curves were in the range of 0.54 to 0.64 eV for all the samples throughout the entire investigated time-frame. This indicates that the conduction mechanism is not significantly changed during the investigated time-frame. Since the thickness of the outer spinel layer remains relatively constant and since the outer spinel is expected to be far more conductive, it is reasonable to propose that the increase in ASR is due to growth of the chromia scale. Furthermore, a very low ASR value was found after a very short exposure time (2 mΩcm² after 100 h). At this stage of oxide scale evolution, only a very thin chromia layer is expected, so it can be concluded that the resistance of the outer spinel layer is much less than 2 mΩcm² at 850 °C. Interestingly in this context, the ASR values of the copper/iron-coated samples were slightly better than those previously reported for cobalt-coated Sanergy HT samples (see Section 4.2.3). Considering the results of Petric and Ling, the opposite case would be expected, as the conductivity of a copper/iron spinel is lower than that of a cobalt/manganese spinel (see section 2.3.3 and Table 2.2) [43]. However, since the microstructural analysis revealed the presence of substantial amounts of manganese and chromium in the outer spinel, lower ASR values are deemed to be likely, as they may add additional energy levels to the band gap. In addition, a doping effect may occur in the chromia layer when this coating system is used, which appears to be supported by the finding that the activation energies were higher for those samples exposed for longer times than for Sanergy HT

coated with cobalt or cobalt/cerium (See Section 4.2.3).

It was previously mentioned that the usual operational temperature of SOFCs is lower than the exposure temperature at which this material system was tested. While this was done to accelerate degradation, it also led to a thicker oxide scale than one would normally expect in a real fuel cell stack. It has been shown that the chromia scale is significantly less thick when these materials are exposed to lower temperatures [83]. Thus, this coating substrate system would be expected to exhibit significantly better performance when used or exposed at lower temperatures.

4.2.5 Uncoated substrate materials

The electrical properties of two uncoated substrate materials, Sanergy HT and Crofer APU, were characterized. In contrast to AISI 441, these two materials fulfilled the essential requirement for an ASR characterization, i.e., to form a well-adhered oxide layer throughout the entire exposure time-frame. It was found that the measurement of the ASR of uncoated substrate materials, especially of Sanergy HT, was far more challenging than it was for coated materials due to interaction of the platinum paste with the oxide scale, even at very short measurement times. For this reason, the platinum paste "6082" was replaced by platinum paste "6926", both of which are manufactured by Metalor. Platinum paste "6082" contains sintering aids in the form of bismuth, whereas platinum paste "6926" does not contain sintering aids. However, it was not possible to obtain more detailed information about the exact compositions of the two pastes. Paste "6082" was initially selected due to the fact that the sintering procedure required by the manufacturer was at 850 °C for 10 min rather than the corresponding procedure for paste "6926" of "around 1000 °C". In Figure 4.50, ASR values of Sanergy HT measured with the two different pastes and Crofer APU measured with paste "6082" are shown. In Figures 4.51 to 4.53 three representative cross-sections of uncoated samples measured after 1000 h of exposure are shown. Sanergy HT with electrodes of paste "6082" is depicted in Figure 4.51 and it can be seen that there is an area of strong interaction, where break-away oxidation occurred. In Figure 4.52 Crofer APU with the same electrode of paste "6082" is shown; the interaction area in the depicted case is similar. However, based on a visible inspection of all the tested samples, the Crofer APU samples had a lower level of interaction. Figure 4.53 shows an uncoated Sanergy HT sample measured with electrodes of paste "6926" in which there is no evidence of any interaction; this was also the case for all the other uncoated Sanergy HT samples that were measured with paste "6926". The form of interaction was only observed for the uncoated samples and was not at all, or only very locally, observed for the coated samples. Given that most of the coated samples were tested before testing of the uncoated samples, it is not possible to compare directly the results for the uncoated substrate materials with the ASR values of the coated material. The reason why the uncoated substrate material reacted more with the platinum paste than the coated material did remains unclear. It might be due to an effect similar to that described of Dong et al., who reported that platinum

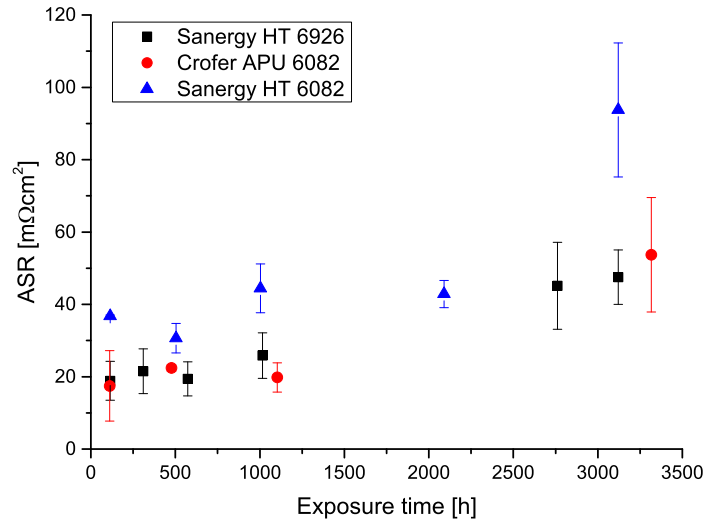


Figure 4.50: Area specific resistance of uncoated substrate material measured with platinum electrodes of different pastes.

applied in thin porous layers enhanced oxidation of pure metals [79]. The fact that the increased oxidation under the platinum electrodes was only visible when coated samples were measured for longer time periods (see section 4.2.2) suggests that the enhanced oxidation effect also applies to coated samples, albeit occurring at a much slower rate. It cannot be ruled out that the platinum interaction is simply an effect of paste "6082" (reflecting the bismuth content of the paste) or that paste "6926" has a similar effect when used for longer time periods. The recommended sintering temperature for paste "6926" is much higher than the temperature used here, so one might expect sintering effects of the electrode when used for longer time periods, which makes reliable ex situ ASR characterization impossible. Future investigations should be performed with platinum pastes, which are suited to low-temperature applications. These pastes are, to the best of the authors knowledge, not yet available commercially.

4.2.6 Conclusion on electrical properties

Measuring the electrical properties proved to be challenging. The interaction of the platinum electrodes with the (uncoated) samples leads to the conclusion that reasonable ASR data can only be obtained when samples are pre-exposed and measured as shortly as possible with platinum electrodes. It is shown that short measurement times generate ASR data that can be successfully linked to the mass gain data, and thus the oxide scale thicknesses of the samples, which is in accordance with the underlying theory. In all the investigated sample systems, it is shown that the chromia scale underneath the spinel top layer contributes most to the ASR value. However,

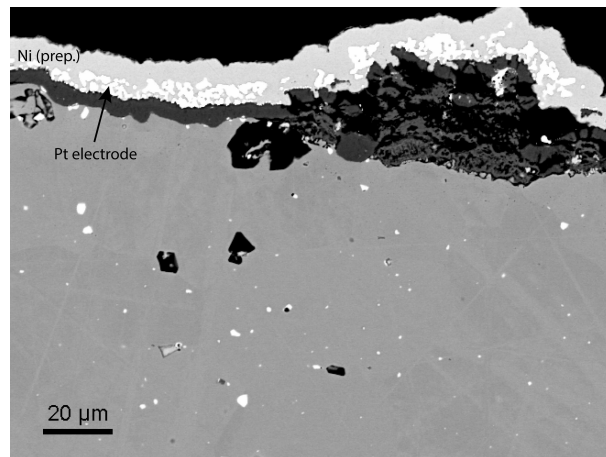


Figure 4.51: Cross-sectional SEM micrograph of a uncoated Sanergy HT sample exposed for 1000 h and measured with platinum ink 6082.

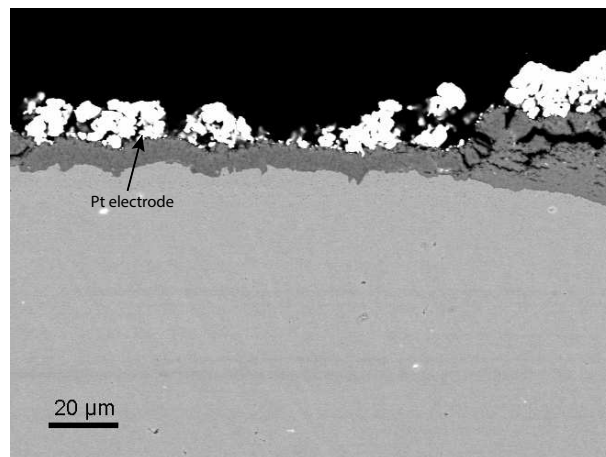


Figure 4.52: Cross-sectional SEM micrograph of a uncoated Crofer APU sample exposed for 1000 h and measured with platinum ink 6082.

the spinel top layer seems to influence also the conductivity mechanism, since different activation energies were observed when, for example, cobalt-coated Sanergy HT was compared to iron/copper-coated Sanergy HT. This suggests that the spinel top coating can, in certain cases, influence the conductivity or the chemical purity of the chromia layer. Apart from the potential impurity effects, one should consider that chromia itself is a very complicated system with respect to electrical conduction, and even slight differences in heat treatment can lead to significant effects on activation energy. Overall, spinel conversion coatings seem to improve the ASR of interconnects and show promise, especially if lower operational temperatures are a priority.

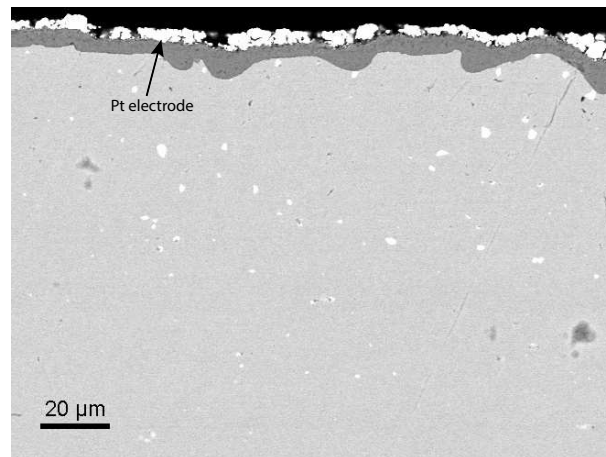


Figure 4.53: Cross-sectional SEM micrograph of a uncoated Sanergy HT sample exposed for 1000 h and measured with platinum ink 6926.

Summary and Outlook

The evaporation of chromium, the corrosion process, and the evolution of the electrical properties of different material systems were investigated during the work for this thesis. Coated ferritic stainless steels were exposed to conditions that simulated the cathode side environment of a solid oxide fuel cell. A unique method for measuring the evaporation of chromium was used, and a strategy was developed to characterize the electronic properties of material systems used as interconnects. Electronic characterization experiments were also performed on simplified model systems of chromia. The main findings of these studies can be summarized as follows:

The denuder technique is proven to be very effective for measuring the volatilization of chromium. Over long exposure times with uncoated AISI 441, standard deviations of less than 1 % were observed and high-level reproducibility was maintained during all the measurements. The investigation of coated AISI 441 in a cathode atmosphere indicates that AISI 441 coated with cerium/cobalt is as effective as comparable commercially available SOFC steels. Reactive-element coatings improve scale adhesion and corrosion resistance but not exert a positive effect in terms of decreasing chromium volatilization. Lanthanum/cobalt-coated AISI 441 samples are not as promising as cerium/cobalt-coated samples due to their lower mechanical stability.

Copper-based conversion coatings on Sandvik Sanergy HT can prevent chromium evaporation. While the manganese/copper coating proved not to be beneficial in terms of mass gain and chromium evaporation at the investigated temperature, the iron- and copper-containing coatings showed good potentials as cathode-side coatings. The coating of copper on iron onto Sanergy HT was further investigated regarding its electrical properties and microstructural evolution. This coating performed slightly better than a conventional cobalt coating.

During this PhD project, a method for ASR characterization was developed, based on a strategy of pre-oxidizing the samples for various times and measuring the ASR

ex situ. This turned out to be advantageous, as it was found that the platinum paste interacted with the oxide scale when the measurement time was too long. The ASR performances of the different coatings can be summarized as follows. When a coating is used that is designed to form a good conductive spinel on the sample surface, the ASR is dominated by the growing chromia scale. This is in line with the theoretical expectations, based on theoretical conductivity values. The most efficient measures for decreasing ASR values are those that decrease the thickness of the chromia layer, e.g., the use of cerium in the coating. However, the conductivity of chromia grown on alloys is not yet fully understood and discrepancies in conductivity values compared to measurements on bulk samples need to be explained.

Future work should be aimed at lower exposure temperatures and different heat treatments, such as pre-oxidation, to optimize the conductivity of the chromia layer. Furthermore, coatings with iron and copper should be optimized with regards to thickness and the iron-to-copper ratio.

REFERENCES

- [1] Scott Hardman, Amrit Chandan, and Robert Steinberger-Wilckens. Fuel cell added value for early market applications, 2015.
- [2] P.-F Nagel. *Electricity from wood through the combination of gasification and solid oxide fuel cells*. PhD thesis, ETH Zurich, 2008.
- [3] I. Staffell, A. Ingram, and K. Kendall. Energy and carbon payback times for solid oxide fuel cell based domestic chp, 2012. *Int. J. Hydrog. Energy*.
- [4] T. D. Hall, H. A. McCrabb, J. Wu, H. Zhang, X. Liu, and E. J. Taylor. Electrodeposition of comn onto stainless steels interconnects for increased lifetimes in sofcs. In S. C. Singhal and K. Eguchi, editors, *Solid Oxide Fuel Cells 12*, volume 35, pages 2489–2502. Electrochemical Society Inc, Pennington, 2011.
- [5] W. J. Quadackers, J. Piron-Abellan, V. Shemet, and L. Singheiser. Metallic interconnectors for solid oxide fuel cells - a review. *Materials at High Temperatures*, 20(2):115–127, 2003. *Mater. High Temp.*
- [6] S. M. Haile. Fuel cell materials and components. *Acta Materialia*, 51(19):5981–6000, 2003. *Acta Mater.*
- [7] R. M. Ormerod. Solid oxide fuel cells. *Chemical Society Reviews*, 32(1):17–28, 2003. *Chem. Soc. Rev.*
- [8] N. Q. Minh. Ceramic fuel-cells. *Journal of the American Ceramic Society*, 76(3):563–588, 1993. *J. Am. Ceram. Soc.*
- [9] R. Pornprasertsuk, P. Ramanarayanan, C. B. Musgrave, and F. B. Prinz. Predicting ionic conductivity of solid oxide fuel cell electrolyte from first principles. *Journal of Applied Physics*, 98(10), 2005. *J. Appl. Phys.*
- [10] S. C. Singhal. Advances in solid oxide fuel cell technology. *Solid State Ionics*, 135(1-4):305–313, 2000. *Solid State Ion.*
- [11] J. W. Fergus. Metallic interconnects for solid oxide fuel cells. *Materials Science and Engineering a-Structural Materials Properties Microstructure and Processing*, 397(1-2):271–283, 2005. *Mater. Sci. Eng. A-Struct. Mater. Prop. Microstruct. Process.*

- [12] S. Linderoth, P. V. Hendriksen, M. Mogensen, and N. Langvad. Investigations of metallic alloys for use as interconnects in solid oxide fuel cell stacks. *Journal of Materials Science*, 31(19):5077–5082, 1996. J. Mater. Sci.
- [13] H. Y. Tu and U. Stimming. Advances, aging mechanisms and lifetime in solid-oxide fuel cells. *Journal of Power Sources*, 127(1-2):284–293, 2004. J. Power Sources.
- [14] J. W. Fergus. Lanthanum chromite-based materials for solid oxide fuel cell interconnects. *Solid State Ionics*, 171(1-2):1–15, 2004. Solid State Ion.
- [15] P. D. Jablonski, C. J. Cowen, and J. S. Sears. Exploration of alloy 441 chemistry for solid oxide fuel cell interconnect application. *Journal of Power Sources*, 195(3):813–820, 2010. J. Power Sources.
- [16] M. Stanislawski, E. Wessel, K. Hilpert, T. Markus, and L. Singheiser. Chromium vaporization from high-temperature alloys i. chromia-forming steels and the influence of outer oxide layers. *Journal of the Electrochemical Society*, 154(4):A295–A306, 2007. J. Electrochem. Soc.
- [17] R. Sachitanand, M. Sattari, J. E. Svensson, and J. Froitzheim. Evaluation of the oxidation and cr evaporation properties of selected fecr alloys used as sofc interconnects. *International Journal of Hydrogen Energy*, 38(35):15328–15334, 2013. Int. J. Hydrog. Energy.
- [18] Per Kofstad. *High Temperature Corrosion*. Elsevier Applied Science, 1988.
- [19] Michael Schütze. *Protective Oxide Scales and Their Breakdown*. John Wiley & Sons, 1997.
- [20] H. J. T. Ellingham. Reproducibility of oxides and sulfides in metallurgical processes. *Journal of the Society for Chemical Industry*, pages 63–125, 1944.
- [21] <http://oregonstate.edu/instruct/me581/homework/overheads/ellingham.jpg>.
- [22] Niklas Israelsson. High temperature corrosion of fecral alloys, 2013.
- [23] C. Wagner. The theory of the warm-up process. *Zeitschrift Fur Physikalische Chemie-Abteilung B-Chemie Der Elementarprozesse Aufbau Der Materie*, 21(1/2):25–41, 1933. Z. Phys. Chem. B-Chem. Elem. Aufbau. Mater.
- [24] N. Bricks, G. H. Meier, and Pettit F. S. *Introduction to the High-Temperature Oxidation of Metals*. Cambridge University Press, 2009.
- [25] P. Huczowski, N. Christiansen, V. Shemet, J. Pironabellan, L. Singheiser, and W. J. Quadackers. Oxidation limited life times of chromia forming ferritic steels. *Materials and Corrosion-Werkstoffe Und Korrosion*, 55(11):825–830, 2004. Mater. Corros.

- [26] D. E. Alman and P. D. Jablonski. Effect of minor elements and a ce surface treatment on the oxidation behavior of an fe-22cr-0.5mn (crofer 22 apu) ferritic stainless steel. *International Journal of Hydrogen Energy*, 32(16):3743–3753, 2007. Int. J. Hydrog. Energy.
- [27] B. A. Pint. Progress in understanding the reactive element effect since the whittle and stringer literature review. In P. F. Tortorelli, I. G. Wright, and P. Y. Hou, editors, *Proc. John Stringer Symposium on High Temperature Corrosion*,,, Indianapolis, 2003. ASM International, Materials Park, OH, pp. 9-19.
- [28] D. P. Whittle and J. Stringer. Improvements in high-temperature oxidation resistance by additions of reactive elements or oxide dispersions. *Philosophical Transactions of the Royal Society of London Series a-Mathematical Physical and Engineering Sciences*, 295(1413):309–&, 1980. Philos. Trans. R. Soc. Lond. Ser. A-Math. Phys. Eng. Sci.
- [29] S. Fontana, R. Amendola, S. Chevalier, P. Piccardo, G. Caboche, M. Viviani, R. Molins, and M. Sennour. Metallic interconnects for sofc: Characterisation of corrosion resistance and conductivity evaluation at operating temperature of differently coated alloys. *Journal of Power Sources*, 171(2):652–662, 2007. J. Power Sources.
- [30] S. Chevalier, C. Valot, G. Bonnet, J. C. Colson, and J. P. Larpin. The reactive element effect on thermally grown chromia scale residual stress. *Materials Science and Engineering a-Structural Materials Properties Microstructure and Processing*, 343(1-2):257–264, 2003. Mater. Sci. Eng. A-Struct. Mater. Prop. Microstruct. Process.
- [31] W. Qu, L. Jian, J. M. Hill, and D. G. Ivey. Electrical and microstructural characterization of spinel phases as potential coatings for sofc metallic interconnects. *Journal of Power Sources*, 153(1):114–124, 2006. J. Power Sources.
- [32] S. Fontana, S. Chevalier, and G. Caboche. Metallic interconnects for solid oxide fuel cell: Performance of reactive element oxide coating during 10, 20 and 30 months exposure. *Oxidation of Metals*, 78(5-6):307–328, 2012. Oxid. Met.
- [33] B. B. Ebbinghaus. Thermodynamics of gas-phase chromium species - the chromium oxides, the chromium oxyhydroxides, and volatility calculations in waste incineration processes. *Combustion and Flame*, 93(1-2):119–137, 1993. Combust. Flame.
- [34] B. B. Ebbinghaus. Thermodynamics of gas-phase chromium species - the chromium chlorides, oxychlorides, fluorides, oxyfluorides, hydroxides, oxyhydroxides, mixed oxyfluorochlorohydroxides, and volatility calculations in waste incineration processes. *Combustion and Flame*, 101(3):311–338, 1995. Combust. Flame.

- [35] E. J. Opila and publications trans tech. *Volatility of common protective oxides in high-temperature water vapor: Current understanding and unanswered questions*, volume 461-464 of *Materials Science Forum*, pages 765–773. 2004.
- [36] E. J. Opila, D. L. Myers, N. S. Jacobson, I. M. B. Nielsen, D. F. Johnson, J. K. Olminky, and M. D. Allendorf. Theoretical and experimental investigation of the thermochemistry of $\text{cro}_2(\text{oh})(2)(\text{g})$. *Journal of Physical Chemistry A*, 111(10):1971–1980, 2007. J. Phys. Chem. A.
- [37] M. Stanislawski, J. Froitzheim, L. Niewolak, W. J. Quadackers, K. Hilpert, T. Markus, and L. Singheiser. Reduction of chromium vaporization from sofc interconnectors by highly effective coatings. *Journal of Power Sources*, 164(2):578–589, 2007. J. Power Sources.
- [38] H. Kurokawa, C. P. Jacobson, L. C. DeJonghe, and S. J. Visco. Chromium vaporization of bare and of coated iron-chromium alloys at 1073 k. *Solid State Ionics*, 178(3-4):287–296, 2007. Solid State Ion.
- [39] K. Huang, P. Y. Hou, and J. B. Goodenough. Reduced area specific resistance for iron-based metallic interconnects by surface oxide coatings. *Materials Research Bulletin*, 36(1-2):81–95, 2001. Mater. Res. Bull.
- [40] M. R. Ardigo, I. Popa, S. Chevalier, V. Parry, A. Galerie, P. Girardon, F. Perry, R. Laucournet, A. Brevet, and E. Rigal. Coated interconnects development for high temperature water vapour electrolysis: Study in anode atmosphere. *International Journal of Hydrogen Energy*, 38(36):15910–15916, 2013. Int. J. Hydrog. Energy.
- [41] J. Froitzheim and J. E. Svensson. Multifunctional nano-coatings for sofc interconnects. In S. C. Singhal and K. Eguchi, editors, *Solid Oxide Fuel Cells 12*, volume 35, pages 2503–2508. Electrochemical Society Inc, Pennington, 2011.
- [42] S. Canovic, J. Froitzheim, R. Sachitanand, M. Nikumaa, M. Halvarsson, L. G. Johansson, and J. E. Svensson. Oxidation of co- and ce-nanocoated fecr steels: A microstructural investigation. *Surface and Coatings Technology*, 215(0):62–74, 2013.
- [43] A. Petric and H. Ling. Electrical conductivity and thermal expansion of spinels at elevated temperatures. *Journal of the American Ceramic Society*, 90(5):1515–1520, 2007. J. Am. Ceram. Soc.
- [44] Smart and Moore. *Solid State Chemistry*. Taylor and Francis Group, 2005.
- [45] A. Holt and P. Kofstad. Electrical-conductivity and defect structure of cr_2o_3 .2. reduced temperatures (less-than-similar-to-1000-degrees-c). *Solid State Ionics*, 69(2):137–143, 1994. Solid State Ion.

- [46] D. B. Meadowcroft and F. G. Hicks. Electrical conduction processes and defect structure of chromic oxide. *Proc. Br. Ceram. Soc.*, 23:33–41, 1972.
- [47] F. Lebreau, M. M. Islam, B. Diawara, and P. Marcus. Structural, magnetic, electronic, defect, and diffusion properties of Cr_2O_3 : A dft+u study. *Journal of Physical Chemistry C*, 118(31):18133–18145, 2014. J. Phys. Chem. C.
- [48] W. C. Hagel and A. U. Seybolt. Cation diffusion in Cr_2O_3 . *Journal of the Electrochemical Society*, 108(12):1146–1152, 1961. J. Electrochem. Soc.
- [49] K. P. Lillerud and P. Kofstad. On high-temperature oxidation of chromium .1. oxidation of annealed, thermally etched chromium at 800-degrees-1100-degrees-c, 1980. J. Electrochem. Soc.
- [50] J. A. Crawford and R. W. Vest. Electrical conductivity of single-crystal Cr_2O_3 . *Journal of Applied Physics*, 35(8):2413–&, 1964. J. Appl. Phys.
- [51] H. Nagai, T. Fujikawa, and K. Shoji. Electrical-conductivity of Cr_2O_3 doped with La_2O_3 , Y_2O_3 and NiO . *Transactions of the Japan Institute of Metals*, 24(8):581–588, 1983.
- [52] J. H. Park and K. Natesan. Electronic transport in thermally grown Cr_2O_3 . *Oxidation of Metals*, 33(1-2):31–54, 1990. Oxid. Met.
- [53] A. Holt and P. Kofstad. Electrical-conductivity and defect structure of Cr_2O_3 .1. high-temperatures (greater-than-similar-to-1000-degrees-c). *Solid State Ionics*, 69(2):127–136, 1994. Solid State Ion.
- [54] K. A. Hay, F. G. Hicks, and D. R. Holmes. The transport properties and defect structure of the oxide $(\text{Fe, Cr})_2\text{O}_3$ formed on Fe-Cr alloys. *Materials and Corrosion*, 21(11):917–924, 1970.
- [55] Y. Larring, R. Haugsrud, and T. Norby. Ht corrosion of a Cr-5 wt the oxide scale - effects of water vapor, 2003. J. Electrochem. Soc.
- [56] K. Q. Huang, P. Y. Hou, and J. B. Goodenough. Characterization of iron-based alloy interconnects for reduced temperature solid oxide fuel cells, 2000. Solid State Ion.
- [57] S. Chevalier, G. Caboche, K. Przybylski, and T. Brylewski. Effect of nano-layered ceramic coatings on the electrical conductivity of oxide scale grown on ferritic steels. *Journal of Applied Electrochemistry*, 39(4):529–534, 2009. J. Appl. Electrochem.
- [58] Z. G. Lu, J. H. Zhu, E. A. Payzant, and M. P. Paranthaman. Electrical conductivity of the manganese chromite spinel solid solution. *Journal of the American Ceramic Society*, 88(4):1050–1053, 2005. J. Am. Ceram. Soc.

- [59] Sofia Karlsson. High temperature corrosion of stainless steels, 2011.
- [60] Matthew P Dewar. Characterization and evaluation of aged 20cr32ni1nb stainless steels. Master's thesis, University of Alberta, 2013.
- [61] K. L. Scrivener. Backscattered electron imaging of cementitious microstructures: understanding and quantification. *Cement & Concrete Composites*, 26(8):935–945, 2004. Cem. Concr. Compos.
- [62] Henrik Asteman. *Water Vapour Induced Active Oxidation of Stainless Steel*. PhD thesis, University of Gothenburg, 2002.
- [63] J. Froitzheim, H. Ravash, E. Larsson, L. G. Johansson, and J. E. Svensson. Investigation of chromium volatilization from fecr interconnects by a denuder technique. *Journal of the Electrochemical Society*, 157(9):B1295–B1300, 2010. J. Electrochem. Soc.
- [64] J. Froitzheim, S. Canovic, M. Nikumaa, R. Sachitanand, L. G. Johansson, and J. E. Svensson. Long term study of cr evaporation and high temperature corrosion behaviour of co coated ferritic steel for solid oxide fuel cell interconnects. *Journal of Power Sources*, 220:217–227, 2012. J. Power Sources.
- [65] J. Froitzheim, A. Magraso, T. Holt, M. W. Lundberg, H. F. Windisch, R. Berger, R. Sachitanand, J. Westlinder, J. E. Svensson, and R. Haugsrud. Nano coated interconnects for sofc (nacosofc). *Solid Oxide Fuel Cells 13 (Sofc-Xiii)*, 57(1):2187–2193, 2013.
- [66] Z. G. Yang, G. G. Xia, C. M. Wang, Z. M. Nie, J. Templeton, J. W. Stevenson, and P. Singh. Investigation of iron-chromium-niobium-titanium ferritic stainless steel for solid oxide fuel cell interconnect applications. *Journal of Power Sources*, 183(2):660–667, 2008. J. Power Sources.
- [67] W. N. Liu, X. Sun, E. Stephens, and M. Khaleel. Interfacial shear strength of oxide scale and ss 441 substrate. *Metallurgical and Materials Transactions a-Physical Metallurgy and Materials Science*, 42A(5):1222–1228, 2011. Metall. Mater. Trans. A-Phys. Metall. Mater. Sci.
- [68] N. Shaigan, W. Qu, D. G. Ivey, and W. X. Chen. A review of recent progress in coatings, surface modifications and alloy developments for solid oxide fuel cell ferritic stainless steel interconnects. *Journal of Power Sources*, 195(6):1529–1542, 2010. J. Power Sources.
- [69] I. Belogolovsky, P. Y. Hou, C. P. Jacobson, and S. J. Visco. Chromia scale adhesion on 430 stainless steel: Effect of different surface treatments. *Journal of Power Sources*, 182(1):259–264, 2008. J. Power Sources.

- [70] P. Y. Hou and J. Stringer. The effect of reactive element additions on the selective oxidation, growth and adhesion of chromia scales. *Materials Science and Engineering a-Structural Materials Properties Microstructure and Processing*, 202(1-2):1–10, 1995. Mater. Sci. Eng. A-Struct. Mater. Prop. Microstruct. Process.
- [71] M. Casteel, D. Lewis, P. Willson, and M. Alinger. Ionic conductivity method for measuring vaporized chromium species from solid oxide fuel cell interconnects. *International Journal of Hydrogen Energy*, 37(8):6818–6829, 2012. Int. J. Hydrog. Energy.
- [72] P. Wei, M. R. Bateni, and A. Petric. Conversion of copper and manganese metallic films to spinel coating. *Journal of Materials Science*, 47(13):5205–5215, 2012. J. Mater. Sci.
- [73] S. C. Paulson, M. R. Bateni, P. Wei, A. Petric, and V. I. Birss. *Improving LSM Cathode Performance Using (Cu,Mn)(3)O(4) Spinel Coated UNS430 Ferritic Stainless Steel SOFC Interconnects*, volume 7 of *ECS Transactions*, pages 1097–1106. 2007.
- [74] L. M. Salah, A. M. Moustafa, and I. S. Ahmed Farag. Structural characteristics and electrical properties of copper doped manganese ferrite. *Ceramics International*, 38(7):5605–5611, 2012.
- [75] X. Chen, P. Y. Hou, C. P. Jacobson, S. J. Visco, and L. C. De Jonghe. Protective coating on stainless steel interconnect for sofc: oxidation kinetics and electrical properties. *Solid State Ionics*, 176(5-6):425–433, 2005. Solid State Ion.
- [76] A. W. B. Skilbred and R. Haugsrud. Sandvik sanergy ht - a potential interconnect material for lanbo4-based proton ceramic fuel cells. *Journal of Power Sources*, 206:70–76, 2012. J. Power Sources.
- [77] K. Kawamura, T. Nitobe, H. Kurokawa, M. Ueda, and T. Maruyama. Effect of electric current on growth of oxide scale on fe-25cr alloy for sofc interconnect at 1073 k. *Journal of the Electrochemical Society*, 159(3):B259–B264, 2012. J. Electrochem. Soc.
- [78] P. Kodjamanova, Q. X. Fu, and L. Gautier. Electric current effects on the corrosion behaviour of high chromium ferritic steels. *Oxidation of Metals*, 79(1-2):53–64, 2013. Oxid. Met.
- [79] Q. Dong, G. Hultquist, G. I. Sproule, and M. J. Graham. Platinum-catalyzed high temperature oxidation of metals. *Corrosion Science*, 49(8):3348–3360, 2007. Corrosion Sci.
- [80] Y. J. Liu, J. W. Fergus, and C. Dela Cruz. Electrical properties, cation distributions, and thermal expansion of manganese cobalt chromite spinel oxides.

-
- Journal of the American Ceramic Society*, 96(6):1841–1846, 2013. J. Am. Ceram. Soc.
- [81] Y. J. Liu, J. W. Fergus, K. L. Wang, and C. Dela Cruz. Crystal structure, chemical stabilities and electrical conductivity of fe-doped manganese cobalt spinel oxides for sofc interconnect coatings. *Journal of the Electrochemical Society*, 160(11):F1316–F1321, 2013. J. Electrochem. Soc.
- [82] T. Kiefer, M. Zahid, F. Tietz, D. Stoever, and H. R. Zeffass. Electrical conductivity and thermal expansion coefficients of spinels in the series $\text{mnco}_2\text{-xfexo}_4$ for application as a protective layer in sofc. pages 261–266. Risoe National Laboratory, 2005.
- [83] Hannes Falk-Windisch, Jan Erik Svensson, and Jan Froitzheim. The effect of temperature on chromium vaporization and oxide scale growth on interconnect steels for solid oxide fuel cells. *Journal of Power Sources*, 287(0):25–35, 2015.